

Measuring coalescing massive binary black holes with gravitational waves: The impact of spin-induced precession

Ryan N. Lang and Scott A. Hughes

Department of Physics and MIT Kavli Institute, MIT, 77 Massachusetts Avenue, Cambridge, Massachusetts 02139, USA
(Received 11 August 2006; published 1 December 2006)

The coalescence of massive black holes generates gravitational waves (GWs) that will be measurable by space-based detectors such as LISA to large redshifts. The spins of a binary's black holes have an important impact on its waveform. Specifically, geodetic and gravitomagnetic effects cause the spins to precess; this precession then modulates the waveform, adding periodic structure which encodes useful information about the binary's members. Following pioneering work by Vecchio, we examine the impact upon GW measurements of including these precession-induced modulations in the waveform model. We find that the additional periodicity due to spin precession breaks degeneracies among certain parameters, greatly improving the accuracy with which they may be measured. In particular, mass measurements are improved tremendously, by one to several orders of magnitude. Localization of the source on the sky is also improved, though not as much—low redshift systems can be localized to an ellipse which is roughly $10 - a\ few \times 10$ arcminutes in the long direction and a factor of 2 smaller in the short direction. Though not a drastic improvement relative to analyses which neglect spin precession, even modest gains in source localization will greatly facilitate searches for electromagnetic counterparts to GW events. Determination of distance to the source is likewise improved: We find that relative error in measured luminosity distance is commonly $\sim 0.1\% - 0.4\%$ at $z \sim 1$. Finally, with the inclusion of precession, we find that the magnitude of the spins themselves can typically be determined for low redshift systems with an accuracy of about $0.1\% - 10\%$, depending on the spin value, allowing accurate surveys of mass and spin evolution over cosmic time.

DOI: [10.1103/PhysRevD.74.122001](https://doi.org/10.1103/PhysRevD.74.122001)

PACS numbers: 04.80.Nn, 04.25.Nx, 04.30.Db

I. INTRODUCTION

A. Background to this analysis

Observations have now demonstrated that massive black holes are ubiquitous in the local universe. It appears that all galaxies with central bulges contain black holes whose masses are strongly correlated with the properties of the bulge [1,2]. Hierarchical structure formation teaches us that these galaxies assembled over cosmic history through the repeated coalescence of the dark matter halos in which they reside [3]. Taken together, these suggest that coalescences of massive black holes should be relatively frequent events, especially at high redshift when halo coalescences were common [4].

Massive black hole coalescences are extremely strong gravitational wave (GW) sources. In the relevant mass band—thousands to millions of solar masses—the GWs these binaries generate are at low frequency ($f \sim 10^{-4.5} - 10^{-1}$ Hz) where ground-based GW antennae have poor sensitivity due to geophysical and other terrestrial noise sources. Measuring GWs from massive black holes requires going into the quiet environment of space. LISA, the Laser Interferometer Space Antenna, is being designed as a joint NASA-ESA mission to measure GWs in this frequency band; cosmological massive black hole coalescences are among its highest priority targets. By measuring these GWs, one can infer the properties of the source that generated the waves. Some particularly important and interesting properties are the masses of the binary's mem-

bers, their spins, the binary's location on the sky, and its distance from the solar system barycenter. Measuring a population of coalescence events could thus provide a wealth of data on the cosmological distribution and evolution of black hole masses and spins.

Most analyses of how well binary black hole parameters can be determined by LISA measurements have ignored the impact of spin-induced precession [5–7]. Under such an assumption, subsets of parameters can be highly correlated with each other, increasing the errors in parameter estimation. One such subset comprises the binary's “chirp mass” \mathcal{M} , its reduced mass μ , and the spin parameters β and σ (which are written out explicitly in Sec. II A). These four parameters influence the GW phase Φ . As discussed in [8,9], the correlation coefficient between μ and β is nearly 1. It is thus difficult to “detangle” these parameters from one another in a measurement.

Another such subset consists of a binary's sky position, orientation, and distance. To see why these parameters are strongly correlated, consider the form of the two polarizations of the strongest quadrupole harmonic of the gravitational waveform:

$$h_+(t) = 2 \frac{\mathcal{M}^{5/3} (\pi f)^{2/3}}{D_L} (1 + \cos^2 \iota) \cos \Phi(t), \quad (1.1)$$

$$h_\times(t) = -4 \frac{\mathcal{M}^{5/3} (\pi f)^{2/3}}{D_L} \cos \iota \sin \Phi(t). \quad (1.2)$$

(We work in units with $G = 1 = c$; a convenient conver-

sion factor in this system is $10^6 M_\odot = 4.92$ seconds.) The quantity ι is the binary's inclination relative to the line of sight: $\cos \iota \equiv \hat{\mathbf{L}} \cdot \hat{\mathbf{n}}$, where $\hat{\mathbf{L}}$, the direction of the binary's orbital angular momentum, defines its orientation and $\hat{\mathbf{n}}$ is the direction from observer to source. The quantity D_L is the luminosity distance to the source, and $f(t) \equiv (1/2\pi)d\Phi/dt$.

One does not measure the polarizations h_+ and h_\times directly; rather, one measures a sum $h_M(t)$ in which the two polarizations are weighted by antenna response functions as follows:

$$h_M(t) = F_+(\theta_N, \phi_N, \psi_N)h_+(t) + F_\times(\theta_N, \phi_N, \psi_N)h_\times(t). \quad (1.3)$$

(This equation should be taken as schematic; see Sec. II C for a more detailed and definitive description.) The angles θ_N and ϕ_N denote the location of the source on the sky in some appropriate coordinate system. The angle ψ_N , known as the ‘‘polarization angle,’’ fixes the orientation of the component of $\hat{\mathbf{L}}$ perpendicular to the line of sight. (In other words, $\hat{\mathbf{L}}$ is fixed by ι and ψ_N .)

Measuring the phase determines chirp mass with high accuracy; the fractional error in \mathcal{M} is often $\sim 10^{-3}$ – 10^{-4} . As far as amplitude is concerned, the chirp mass can be regarded as measured exactly. What remains is to determine, from the measured amplitude and the known \mathcal{M} , the angles θ_N , ϕ_N , ψ_N , ι , and the distance D_L .

As Eqs. (1.1), (1.2), and (1.3) illustrate, these five parameters are strongly correlated. The motion of LISA around the sun¹ breaks these degeneracies to some extent—the angles θ_N and ϕ_N appearing in Eq. (1.3) can be regarded as best defined in a coordinate system tied to LISA. As the antenna orbits the sun, these angles become effectively time dependent. The one-year periodicity imposed by this motion makes it possible to detangle these parameters. Analyses typically find that the position of a merger event at $z \sim 1$ can be determined, on average, to an ellipse which is a degree across in the long direction and a few $\times 10$ arcminutes across in the short direction² [5,7,10]. The distance to such a binary can be determined to 1% accuracy on average (less in some exceptional cases) [6,7,10].

B. Black hole spin and spin precession

The preceding discussion ignores an important piece of relativistic physics: the precession of each binary member's spin vector due to its interaction with the spacetime in which it moves. In general relativity, the spacetime of an isolated object can be regarded as having an ‘‘electric

piece,’’ arising from the object's mass and mass distribution, and a ‘‘magnetic piece,’’ arising from the object's mass currents and their distribution.³ Spin precession consists of a geodetic term, arising from the parallel transport of the spin vector in the gravitoelectric field of the other hole, and Lense-Thirring terms, caused by the gravitomagnetic field of the other hole. The basic physics of gravitomagnetic precession can be simply understood by analogy with a similar (and closely related) electromagnetic phenomenon—the precession of a magnetic dipole $\boldsymbol{\mu}$ immersed in an external magnetic field \mathbf{B} . An object's spin angular momentum \mathbf{S} can be regarded as a gravitational ‘‘magnetic dipole.’’ When immersed in a ‘‘gravitomagnetic field,’’ one finds that \mathbf{S} feels a torque, just as a magnetic dipole $\boldsymbol{\mu}$ experiences a torque when immersed in magnetic field \mathbf{B} . In a binary black hole system, the gravitomagnetic field arises from the binary's orbital motion and the spins of its members. Precession thus includes both spin-orbit (geodetic and orbital gravitomagnetic) and spin-spin effects [12]. (The major goal of the ‘‘Gravity Probe B’’ experiment is to measure the effects of geodetic and spin-spin Lense-Thirring precession upon a gyroscope in low Earth orbit [13].)

As the spins precess, they do so in such a way that the *total* angular momentum $\mathbf{J} = \mathbf{L} + \mathbf{S}_1 + \mathbf{S}_2$ is held constant; the orbital angular momentum \mathbf{L} precesses to compensate for changes in \mathbf{S}_1 and \mathbf{S}_2 . As a consequence, the inclination angle ι and polarization angle ψ_N become time varying (as do certain other quantities appearing in the GW phase function Φ). Figure 1 shows the so-called ‘‘polarization amplitude,’’ defined in Sec. II C, of the waveform measured by a particular detector. Without precession, this quantity is modulated by the orbital motion of LISA, helping to provide some information about the binary's sky position. The polarization amplitude also depends on the angles ι and ψ_N , so it undergoes additional modulation when precession is included. Such precession-imposed time variations quite thoroughly break many of the degeneracies which have been found to limit parameter measurement accuracy in earlier analyses.

It is without a doubt that black holes in nature spin. Observations are not yet precise enough to indicate the value of typical black hole spins; the evidence to date does, however, seem to indicate that fairly rapid rotation is common. For example, the existence of jets from active systems seems to require non-negligible black hole spin—jets appear to be ‘‘launched’’ by the shearing of magnetic field lines (supported by the highly conductive, ionized material accreting onto the black hole) by the differential rotation of spacetime around a rotating black hole [14,15].

¹LISA is being designed as a constellation of three spacecraft whose centroid orbits the sun with a period of one year; see <http://lisa.nasa.gov> for further details.

²It is worth bearing in mind that the full moon subtends an angle of about 30 arcminutes.

³This analogy is most apt in the weak field. In that limit, one can recast the Einstein field equations of general relativity into a form quite similar to Maxwell's equations; see [11] for a detailed discussion. Though the analogy does not fit quite so well in strong field regions, it remains accurate enough to be useful.

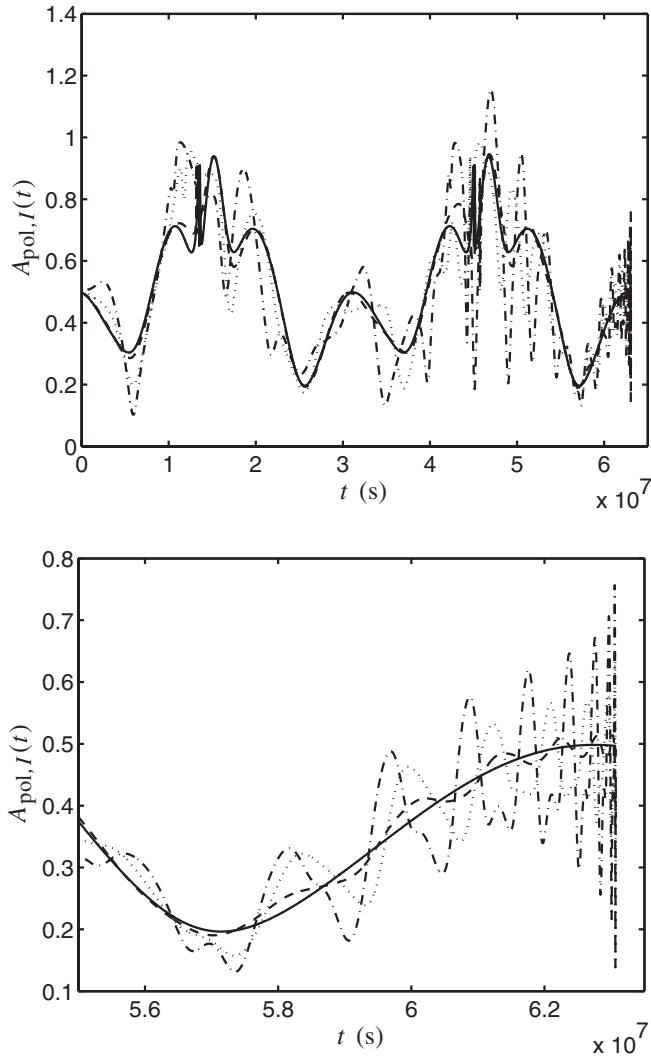


FIG. 1. These figures depict the “polarization amplitude” $A_{\text{pol},I}(t)$ of the signal measured in detector I as a function of time. The curves are as follows: solid line, $\chi_1 = \chi_2 = 0$; dashed line (nearly overlapping the solid line), $\chi_1 = \chi_2 = 0.1$; dotted line, $\chi_1 = \chi_2 = 0.5$; and dot-dashed line, $\chi_1 = \chi_2 = 0.9$. ($\chi = S/m^2$ is the dimensionless spin parameter.) The top figure covers the last two years of inspiral. The spinless curve has periodicity of one year, corresponding to the motion of LISA around the sun. Notice that, as spin is introduced, the curves become more strongly modulated, with the number of additional oscillations growing as the spin is increased. By tracking these spin-precession-induced modulations, it becomes possible to better measure parameters like mass and sky position and to measure spin for the first time. The bottom figure shows a close-up of the final months of inspiral.

Also, observations of highly distorted iron K- α lines—a very sharp fluorescence feature in the rest frame of the emitting iron ions—indicate that this emission is coming from very deep within a gravitational potential (at radii less than the Schwarzschild innermost radius $6M$) and is smeared by near luminal relativistic speeds to boot [16]. Though perhaps influenced somewhat by selection ef-

fects,⁴ these pieces of evidence are strong hints that the black holes which will form the binaries we hope to measure will be strongly influenced by spin.

The only limit in which spin precession can be neglected is that in which the spins of the binary’s members are exactly parallel (or antiparallel) to one another and to the orbital angular momentum \mathbf{L} . Since the target binaries of this analysis are created by galactic merger processes, their members will almost certainly have no preferred alignment—random spin and orbit orientation is expected to be the rule. (This expectation is borne out by work [18] showing that jets in active galaxies are oriented randomly with respect to the disks of their host galaxies.) Taking into account spin precession is thus of paramount importance for GW observations of merging black hole systems.

A great deal of work has gone into developing families of model waveforms (“templates”) sufficiently robust to detect GWs from spinning and precessing binaries, at least in the context of measurements by ground-based detectors [19–25]. The key issue in this case is that the various modulations on the waveform imposed by the binary’s precession smear its power over a wider spectral range, making it much more difficult to detect at the (relatively) low signal-to-noise ratios (SNRs) expected for ground-based observations. Not as much work has gone into the complementary problem of *measuring* these waves—examining the impact precession has upon the precision with which binary properties may be inferred from the waves. To date, the most complete and important analysis of this type is that of Vecchio [26]. Vecchio focuses (for simplicity) on equal mass binaries and only includes the leading “spin-orbit” precession term. This limit is particularly nice as a first analysis of this problem, since it can be treated (largely) analytically (cf. discussion in Sec. III B of Ref. [26]).

Vecchio’s work largely confirms the intuitive expectation discussed above—the precision with which masses are measured is substantially improved; in particular, the reduced mass of the system can be measured with several orders of magnitude more accuracy. Parameters such as the sky location of the binary and the luminosity distance are also measured more accurately, but only by a factor of 2–10.

C. This analysis

Our goal here is to update Vecchio’s pioneering analysis by taking the precession equations and the wave phase to the next higher order and by performing a broader parameter survey (including the impact of mass ratio). By taking the precession equations to higher order, we include “spin-spin” effects—precessional effects due to one black hole’s

⁴The systems for which we have constraints on spin are systems which are actively accreting, and, *ipso facto*, those which are most likely to be rapidly spinning [17].

spin interacting with gravitomagnetic fields from the other hole’s spin. By taking the wave phase to higher order, we include, among other terms, a time-dependent spin-spin interaction. Finally, when the mass ratio differs from 1, the geodetic spin-orbit term causes the two spins to precess at different rates, even without the spin-spin corrections.

Including these effects means that we *cannot* model the precession with a simple, analytic rule—we are forced to integrate the equations of precession numerically as inspiral proceeds, incurring a significant performance cost. Fortunately, the basic “engine” on which this code is based [6] runs extremely fast, thanks largely to the use of spectral integrators (which, in turn, is thanks to a suggestion by E. Berti [7]), so total run time remains reasonable.

The cost in efficiency due to the inclusion of higher-order effects is offset by the more complete description of the signal they provide. An important consequence is that it now becomes possible from GW measurements to determine the spin of each member of the binary. With Vecchio’s approximations, only three components of the black holes’ vector spins can be determined—enough to constrain, but not determine, their spin magnitudes. Our more general approach allows us to measure all six vector spin components. To our knowledge, this is the first analysis indicating how well spin can be measured from merging comparable mass binary systems. (As Barack and Cutler have shown [27], spin is very well determined by measurements of GWs from *extreme mass ratio* binaries—those in which the system’s mass ratio $m_2/m_1 \lesssim 10^{-4}$ or so.)

Our error estimates are computed using the maximum likelihood formalism first introduced in the context of GW measurements by Finn [28]. A potential worry is that we are using a Gaussian approximation to the likelihood function. This approximation is very convenient since it allows us to directly compute a Fisher information matrix. Its inverse is the covariance matrix, which directly encodes the estimated 1- σ errors in measured parameters, as well as correlations among different parameters. The Gaussian approximation is known to be accurate when the SNR is “high enough” [8,28].

Unfortunately, it is not particularly obvious what “high enough” really means. In our case, we are estimating measurement errors on 15 parameters⁵—a rather fearsome number to fit. The Gaussian approximation almost certainly *underestimates* measurement error, since it assumes the likelihood function is completely determined by its curvature in the vicinity of a maximum, missing the possibility of a long tail to large error. We thus fear that our estimates are likely to be optimistic, especially for events with relatively small SNR. It would be quite salubrious to

“spot check” a few cases by directly computing the likelihood function in a few important corners of parameter space and comparing to the Gaussian predictions. This would both quantify the degree to which our calculations are too optimistic and help to determine how large SNR must be for this approximation to be reliable.

In addition to concerns about the Gaussian approximation, it must be noted that the waveform family we use for our analysis is somewhat limited. We use a post-Newtonian description of the GWs from these binaries. Since our analysis requires us to follow these binaries deep into the strong field where the usual post-Newtonian expansion is likely to be somewhat unreliable, it is likely that we are introducing some systematic error. In particular, the equations of spin precession that we are using are only given to the leading order needed to see spin-orbit and spin-spin precession effects [29]. Higher spin-orbit corrections to the equations of motion and precession have recently been derived [30], as have their impact on the waves’ phasing [31]. Another analysis [32] has worked out higher-order spin-spin corrections to the post-Newtonian metric, from which it would not be too difficult to work out equations of motion and precession and then the modification to the waves’ phase. It would be interesting to see what effect the higher-order corrections have on these results.

Finally, it should be noted that the frequency domain expression of the signal which we are using is derived formally using a “stationary phase” approximation. This approximation is based on the idea that the binary’s orbital frequency is changing “slowly.” The orbital frequency is thus well defined over “short” time scales. Quantitatively, this amounts to a requirement that the time scale on which radiation reaction changes the orbital frequency, T_{insp} , be much longer than an orbital period, T_{orb} . Precession introduces a new time scale, T_{prec} , the time it takes for the angular momentum vectors to significantly change their orientations. For the stationary phase approximation to be accurate, we must in addition require $T_{\text{prec}} \gg T_{\text{orb}}$, a somewhat more stringent requirement than $T_{\text{insp}} \gg T_{\text{orb}}$. No doubt, a certain amount of error is introduced due to the breakdown of this condition late in the inspiral.

Thus, the results which we present here should be taken as *indicative* of how well LISA is likely to be able to measure the parameters of massive black hole binaries, but cannot be considered definitive. We are confident, however, that the *improvement* in measurement accuracy obtained by taking spin precession into account is robust. Specifically, we see that errors in masses are reduced dramatically, from one to several orders of magnitude. Errors in sky position and distance are also reduced, but by a smaller factor. Such improvement may nonetheless critically improve the ability of LISA to interface with electromagnetic observatories [33–35]. Finally, the added information in the precession signal allows us to measure the spins of the holes. These improvements due to preces-

⁵Two masses; 2 angles specifying the initial orientation of the binary’s orbit; 4 angles specifying the initial orientation of the spins; 2 spin magnitudes; the time at which coalescence occurs; the phase at coalescence; 2 angles specifying the binary’s position on the sky; and the distance to the binary.

sion will certainly survive and play an important role even in an analysis which addresses the caveats we list above.

D. Organization of this paper

The remainder of the paper is organized as follows. In Sec. II, we discuss the gravitational waveform generated by binary black hole coalescence, focusing upon the slow, adiabatic inspiral. Section II A describes the “intrinsic” waveform produced by the motion of the orbiting black holes as given in the “restricted post-Newtonian expansion” of general relativity. Section II B then describes the post-Newtonian precession equations which we use to model the evolution of the spins of a binary’s members, as well as how those precessions influence the waveform. Finally, in Sec. II C we describe “extrinsic” effects which enter the measured waveform through its measurement by the LISA constellation.

In Sec. III we summarize our parameter estimation formalism; this section will be largely a review to readers familiar with the literature on GW measurements. Section III A first summarizes the maximum likelihood formalism we use to estimate measurement errors. In Sec. III B, we then describe the up-to-date model for the noise which we expect to accompany LISA measurements.

Section IV presents our results. After describing some critical procedural issues in the setup of our calculations in Sec. IV A, we summarize our results for parameters intrinsic to the binary (particularly masses and spins) in Sec. IV B and for extrinsic parameters (particularly sky position and luminosity distance) in Sec. IV C. In both cases, we compare, when appropriate, to results from a code which does not incorporate spin-precession physics. (This code was originally developed for the analysis presented in Ref. [6].) The general rule of thumb we find is that the accuracy with which masses can be determined is improved by about one to several orders of magnitude when precession physics is taken into account. In addition, we find that for low redshift ($z \sim 1$) binaries LISA should be able to determine the spins of the constituent black holes with a relative precision of 0.1%–10%, depending (rather strongly) on the spin value. Likewise, we find improvement in the measurement accuracy of extrinsic parameters, though not quite as striking—half an order of magnitude improvement in source localization and distance determination is a good, rough rule of thumb.

An important consequence of these improvements is that LISA should be able to localize low redshift binaries—using GW measurements alone—to an elliptical “pixel” that is perhaps 10 – a few $\times 10$ arcminutes across in its widest direction and about a factor of 2 smaller along its minor axis. For higher redshift binaries ($z \sim 3$ –5), this pixel is several times larger, perhaps a degree to a few degrees in the long direction and tens of arcminutes to a degree or two in the narrow one. These results suggest that it should not be too arduous a task to search for electro-

magnetic counterparts to a merging binary black hole’s GW signal [33–35]—particularly at low redshift, these pixel sizes are comparable to the field of view of planned large scale surveys.

A concluding and summarizing discussion is given in Sec. V. Along with summarizing our major results and findings, we discuss future work which could allow us to quantitatively assess the consequences of some of the simplifying assumptions we have made.

At several points in this analysis, we need to convert between a source’s redshift z and luminosity distance D_L . To make this conversion, we assume a flat cosmology ($\Omega_{\text{total}} = 1$) with contributions from matter ($\Omega_M = 0.25$) and from a cosmological constant (equation of state parameter $w = -1$, $\Omega_\Lambda = 0.75$). We also choose a Hubble constant $H_0 = 75 \text{ km s}^{-1} \text{ Mpc}^{-1}$. These choices are in concordance with the latest fits presented by the WMAP team in their three-year analysis of the cosmic microwave background [36]. The luminosity distance as a function of redshift is then given by

$$D_L(z) = \frac{(1+z)c}{H_0} \int_0^z \frac{dz'}{\sqrt{\Omega_M(1+z')^3 + \Omega_\Lambda}}. \quad (1.4)$$

II. GRAVITATIONAL WAVES FROM BINARY BLACK HOLE INSPIRAL

The coalescence of a black hole binary can be divided into three stages: (1) an adiabatic inspiral, (2) a merger, and (3) a ringdown, when the resulting black hole settles down to its final state. In this paper, we will focus on the inspiral. Ringdown waves have been analyzed in other work [6,28,37,38]; the most comprehensive recent analysis was performed by Berti, Cardoso, and Will [39]. The merger waveform, describing the strong field and (potentially) violent process of the two black holes merging into a single body, has historically been poorly understood. Recent breakthroughs in numerical relativity may soon correct this [40–42].

The inspiral waveform which will be measured by LISA is a combination of the intrinsic waveform created by the source and extrinsic features related to its location on the sky and modulation effects caused by the motion of the detector. In this section we review the relevant physics involved in the construction of the waveform.

For sources at cosmological distances, all time scales redshift by a factor $1+z$. In the $G=c=1$ units that we use, all factors of mass enter as time scales; thus, masses are redshifted by this $1+z$ factor. [Likewise, quantities such as spin which have dimension (time)² acquire a factor $(1+z)^2$, etc.] In the equations written below, we do not explicitly write out these redshift factors; they should be taken to be implicit in all our equations. When discussing results, we will always quote masses as they would be measured in the rest frame of the source, with redshift given separately.

A. Intrinsic waveform

We treat the members of our binary as moving on quasicircular orbits; eccentricity is very rapidly bled away by gravitational radiation reaction [43], so it is expected that these binaries will have essentially zero eccentricity by the time they enter LISA's frequency band (at least at the mass ratios we consider in this paper, $1 \leq m_1/m_2 \leq 10$). We use the post-Newtonian formalism, an expansion in internal gravitational potential U and internal source velocity v , to build our waveforms. A detailed review of the post-Newtonian formalism can be found in the article by Blanchet [44]; the key pieces which we will use can be found in Refs. [44–48].

The post-Newtonian equations of motion, taken to second post-Newtonian (2PN) order, yield the following generalization of Kepler's third law relating orbital angular frequency Ω and orbital radius (in harmonic coordinates) r [46]:

$$\begin{aligned} \Omega^2 = & \frac{M}{r^3} \left[1 - (3 - \eta) \left(\frac{M}{r} \right) - \sum_{i=1}^2 \left(2 \frac{m_i^2}{M^2} + 3\eta \right) \right. \\ & \times \frac{\hat{\mathbf{L}} \cdot \mathbf{S}_i}{m_i^2} \left(\frac{M}{r} \right)^{3/2} + \left(6 + \frac{41}{4} \eta + \eta^2 - \frac{3}{2} \frac{\eta}{m_1^2 m_2^2} \right. \\ & \left. \left. \times [\mathbf{S}_1 \cdot \mathbf{S}_2 - 3(\hat{\mathbf{L}} \cdot \mathbf{S}_1)(\hat{\mathbf{L}} \cdot \mathbf{S}_2)] \right) \left(\frac{M}{r} \right)^2 \right]. \end{aligned} \quad (2.1)$$

Here $M = m_1 + m_2$ is the total mass of the system, and $\eta = \mu/M$, where $\mu = m_1 m_2 / M$ is the reduced mass. $\hat{\mathbf{L}}$ is the direction of the orbital angular momentum, and \mathbf{S}_i is the spin angular momentum of black hole i . The magnitude of the spin can be expressed as $S_i = \chi_i m_i^2$, where $0 \leq \chi_i \leq 1$. The leading term is the standard result from Newtonian gravity. The $O(M/r)$ term is the first post-Newtonian correction; this is the same physics that, in solar system dynamics, causes the precession of the perihelion of Mercury. The $O((M/r)^{3/2})$ term contains spin-orbit corrections to the equation of motion. Finally, the $O((M/r)^2)$ term is a 2PN correction, which also includes spin-spin terms. From the equations of motion, the orbital energy of the binary E can also be computed; see [46].

The waveform that we will use is the “restricted” 2PN waveform. This approximation can be understood by writing the waveform (somewhat schematically) as [8]

$$h(t) = \text{Re} \left(\sum_{x,m} h_m^x(t) e^{im\Phi_{\text{orb}}(t)} \right), \quad (2.2)$$

where x labels PN order, m is a harmonic index, and $\Phi_{\text{orb}}(t) = \int^t \Omega(t') dt'$ is the orbital phase. In the restricted post-Newtonian waveform, we throw out all amplitude terms except h_2^0 (the “Newtonian quadrupole” term) but compute $\Phi_{\text{orb}}(t)$ to some specified PN order. The restricted PN approximation is motivated by the fact that matched filtering—matching a signal in noisy data by cross-correlating with a theoretical template—is much more

sensitive to phase information than to the amplitude. Since the h_2^0 harmonic contributes most strongly to the waveform over most of the inspiral, the restricted PN approximation is expected to capture the most important portion of the inspiral waveform. It is worth noting, however, that there is additional information encoded by the harmonics that we are neglecting. Especially for the SNRs expected for typical LISA binary black hole measurements, this additional information could play an important role in measuring source characteristics, as pointed out by Hellings and Moore [49].

At any rate, within the restricted PN approximation, the waveform can be written

$$\begin{aligned} h_{ij}(t, \mathbf{x}) = & - \frac{4\mathcal{M}^{5/3}(\pi f)^{2/3}}{|\mathbf{x}|} \\ & \times \begin{bmatrix} \cos\Phi(t) & \sin\Phi(t) & 0 \\ \sin\Phi(t) & -\cos\Phi(t) & 0 \\ 0 & 0 & 0 \end{bmatrix}, \end{aligned} \quad (2.3)$$

where $|\mathbf{x}|$ is the distance to the binary, $\mathcal{M} = \mu^{3/5} M^{2/5}$ is the “chirp mass” (so called because it largely determines the rate at which the system's frequency evolves, or “chirps”), $f = \Omega/\pi = 2f_{\text{orb}}$ is the GW frequency, and $\Phi(t) = \int^t 2\pi f(t') dt' = 2\Phi_{\text{orb}}$ is the GW phase. We have chosen a coordinate system oriented such that the binary's orbit lies within the xy -plane; this tensor will later be projected onto polarization basis tensors to construct the measured polarizations h_+ and h_\times .

The rate at which the frequency changes due to the emission of gravitational radiation is given by [46]

$$\begin{aligned} \frac{df}{dt} = & \frac{96}{5\pi\mathcal{M}^2} (\pi\mathcal{M}f)^{11/3} \left[1 - \left(\frac{743}{336} + \frac{11}{4} \eta \right) (\pi\mathcal{M}f)^{2/3} \right. \\ & + (4\pi - \beta) (\pi\mathcal{M}f) + \left(\frac{34\,103}{18\,144} + \frac{13\,661}{2016} \eta + \frac{59}{18} \eta^2 \right. \\ & \left. \left. + \sigma \right) (\pi\mathcal{M}f)^{4/3} \right]. \end{aligned} \quad (2.4)$$

Notice that the chirp mass \mathcal{M} dominates the rate of change of f ; the reduced mass μ and parameters β and σ have an influence as well. The parameter β describes spin-orbit interactions and is given by

$$\beta = \frac{1}{12} \sum_{i=1}^2 \left[113 \left(\frac{m_i}{M} \right)^2 + 75 \frac{\mu}{M} \right] \frac{\hat{\mathbf{L}} \cdot \mathbf{S}_i}{m_i^2}. \quad (2.5)$$

The parameter σ describes spin-spin interactions:

$$\sigma = \frac{\mu}{48M(m_1^2 m_2^2)} [721(\hat{\mathbf{L}} \cdot \mathbf{S}_1)(\hat{\mathbf{L}} \cdot \mathbf{S}_2) - 247(\mathbf{S}_1 \cdot \mathbf{S}_2)]. \quad (2.6)$$

Notice that β and σ depend on the angles between the binary's angular momentum and the two spins. In previous analyses which have neglected precession, β and σ are constants; precession makes them time dependent.

Using Eq. (2.4), we can now integrate to find

$$t(f) = t_c - \frac{5}{256} \mathcal{M}(\pi \mathcal{M} f)^{-8/3} \left[1 + \frac{4}{3} \left(\frac{743}{336} + \frac{11}{4} \eta \right) \right. \\ \times (\pi \mathcal{M} f)^{2/3} - \frac{8}{5} (4\pi - \beta) (\pi \mathcal{M} f) + 2 \left(\frac{3058673}{1016064} \right. \\ \left. \left. + \frac{5429}{1008} \eta + \frac{617}{144} \eta^2 - \sigma \right) (\pi \mathcal{M} f)^{4/3} \right]. \quad (2.7)$$

The parameter t_c formally defines the time at which f diverges within the post-Newtonian framework. In reality, we expect finite size effects to significantly modify the binary's evolution as the members come into contact. The system evolves so quickly as the bodies come together that t_c is nonetheless a useful surrogate for a "time of coalescence." Finally, the wave phase $\Phi(t) = \int^t 2\pi f(t') dt'$ as a function of f is given by

$$\Phi(f) = \Phi[t(f)] = \Phi_c - \frac{1}{16} (\pi \mathcal{M} f)^{-5/3} \left[1 + \frac{5}{3} \left(\frac{743}{336} \right. \right. \\ \left. \left. + \frac{11}{4} \eta \right) (\pi \mathcal{M} f)^{2/3} - \frac{5}{2} (4\pi - \beta) (\pi \mathcal{M} f) \right. \\ \left. \left. + 5 \left(\frac{3058673}{1016064} + \frac{5429}{1008} \eta + \frac{617}{144} \eta^2 - \sigma \right) \right. \right. \\ \left. \left. \times (\pi \mathcal{M} f)^{4/3} \right], \quad (2.8)$$

where Φ_c is the phase at time t_c . The restricted PN waveform is then constructed by inserting (2.8) into (2.3).

B. Precession equations

We next examine the effects of precession on the binary system. As discussed in the Introduction, spin-orbit and spin-spin interactions cause the black hole spins \mathbf{S}_1 and \mathbf{S}_2 to precess. Precession occurs, at leading order,⁶ on a time scale $T_{\text{prec}} \propto r^{5/2}$ at large separations [50]. Since this is smaller than the inspiral time scale T_{insp} , we treat the total angular momentum $\mathbf{J} = \mathbf{L} + \mathbf{S}_1 + \mathbf{S}_2$ as constant over T_{prec} . The orbital angular momentum \mathbf{L} must then precess to compensate for changes in \mathbf{S}_1 and \mathbf{S}_2 . Since T_{prec} is longer than the orbital time scale T_{orb} , we use an orbit-averaged version of the precession equations [29]:

$$\dot{\mathbf{S}}_1 = \frac{1}{r^3} \left[\left(2 + \frac{3}{2} \frac{m_2}{m_1} \right) \mu \sqrt{Mr} \hat{\mathbf{L}} \right] \times \mathbf{S}_1 \\ + \frac{1}{r^3} \left[\frac{1}{2} \mathbf{S}_2 - \frac{3}{2} (\mathbf{S}_2 \cdot \hat{\mathbf{L}}) \hat{\mathbf{L}} \right] \times \mathbf{S}_1, \quad (2.9)$$

⁶Several effects are built in to the precession equations discussed below, leading to precessions that occur on time scales scaling as $r^{5/2}$ and r^3 . Since we integrate these equations numerically, all of these effects are included in our analysis. For the purposes of this discussion, we subsume these effects into the leading-order time scale T_{prec} discussed here.

$$\dot{\mathbf{S}}_2 = \frac{1}{r^3} \left[\left(2 + \frac{3}{2} \frac{m_1}{m_2} \right) \mu \sqrt{Mr} \hat{\mathbf{L}} \right] \times \mathbf{S}_2 \\ + \frac{1}{r^3} \left[\frac{1}{2} \mathbf{S}_1 - \frac{3}{2} (\mathbf{S}_1 \cdot \hat{\mathbf{L}}) \hat{\mathbf{L}} \right] \times \mathbf{S}_2, \quad (2.10)$$

where⁷ $r = M^{1/3}/(\pi f)^{2/3}$. These equations each have two pieces [12]. Consider the equation for $\dot{\mathbf{S}}_1$. The first piece, which contains no \mathbf{S}_2 dependence, is the spin-orbit term. This term, which comes in at 1PN order, is due to the geodetic precession of \mathbf{S}_1 as hole 1 orbits in the spacetime generated by the mass of hole 2, and to the Lense-Thirring precession of \mathbf{S}_1 in the gravitomagnetic field generated by the orbital motion of hole 2. The second piece is the spin-spin term, which enters at 1.5PN order. This term can be understood as the Lense-Thirring precession of \mathbf{S}_1 in the gravitomagnetic field generated by the spin of hole 2. Note that the magnitudes of the spins do not change at this order; see [29] for more details. From conservation of total angular momentum on short time scales, we have

$$\dot{\mathbf{L}} = -(\dot{\mathbf{S}}_1 + \dot{\mathbf{S}}_2). \quad (2.11)$$

Over longer time scales, we must also consider the change in total angular momentum due to the radiation reaction, which is given by

$$\dot{\mathbf{J}} = -\frac{32}{5} \frac{\mu^2}{r} \left(\frac{M}{r} \right)^{5/2} \hat{\mathbf{L}} \quad (2.12)$$

to lowest order.

Considering only the spin-orbit terms and taking the limit $S_2 = 0$ or $m_1 = m_2$ leads to a system whose precession can be described analytically; this is the "simple precession" limit described in [29]. Simple precession can be visualized as a rotation of \mathbf{L} and $\mathbf{S} = \mathbf{S}_1 + \mathbf{S}_2$ around the total angular momentum \mathbf{J} . (Since inspiral shrinks \mathbf{J} , the precession is actually around a slightly different direction \mathbf{J}_0 ; see [29] for further discussion.)

Since Vecchio restricts his analysis to $m_1 = m_2$ and does not include the spin-spin interaction, this limit is appropriate for his work [26]. As a consequence, Vecchio takes the quantities $\hat{\mathbf{L}} \cdot \hat{\mathbf{S}}_i$, $\hat{\mathbf{S}}_1 \cdot \hat{\mathbf{S}}_2$, and β to be constant. (He does not include the spin-spin term σ in the analysis.) Here, we will study the impact of the full (albeit orbit-averaged) precession equations, including spin-spin terms, and include the impact of mass ratio. An analytic description is not possible in this case, so we must integrate these equations numerically. The behavior is qualitatively similar to the simple precession case, but with significant quantitative differences. For example, β now oscillates around an average value. For unequal masses (say $m_1/m_2 \gtrsim 2$), the difference due to precession can be substantial [47]. Such cases are also astrophysically the most

⁷We use only the lowest-order Newtonian orbital quantities in these equations. Including more terms would introduce higher-order effects into the precession.

interesting—a mass ratio of roughly 10 is favored in binary black hole formation scenarios arising from hierarchical structure formation [51].

The precession of the orbital plane causes a change in the orbital phase $\Phi_{\text{orb}}(t)$ [29]. Multiplying by a factor of 2, the change in the wave phase is

$$\delta_p \Phi(t) = - \int_t^{t_c} \delta_p \dot{\Phi}(t') dt', \quad (2.13)$$

where

$$\delta_p \dot{\Phi}(t) = \frac{2\hat{\mathbf{L}} \cdot \hat{\mathbf{n}}}{1 - (\hat{\mathbf{L}} \cdot \hat{\mathbf{n}})^2} (\hat{\mathbf{L}} \times \hat{\mathbf{n}}) \cdot \dot{\hat{\mathbf{L}}}, \quad (2.14)$$

and $\hat{\mathbf{n}}$ is the direction of the binary on the sky. At this point, we note that precession has several effects on the observed waveform. It changes the orbital phase, even at Newtonian order, by the amount (2.13), and it modifies the functions β and σ which appear in the post-Newtonian phase (2.8) and time-frequency relation (2.7). In the next section, we consider extrinsic effects on the waveform and find that precession of the orbital plane modifies them as well.

C. Extrinsic effects

We have now constructed the intrinsic GWs emitted by a precessing binary in the restricted post-Newtonian approximation. The waveform measured by LISA will also include extrinsic effects due to the binary's location on the sky and the motion of the detector.

We can write the wave as a combination of two orthogonal polarizations propagating in the $-\hat{\mathbf{n}}$ direction. Define $\hat{\mathbf{p}}$ and $\hat{\mathbf{q}}$ as axes orthogonal to $\hat{\mathbf{n}}$, with $\hat{\mathbf{p}} = \hat{\mathbf{n}} \times \hat{\mathbf{L}}/|\hat{\mathbf{n}} \times \hat{\mathbf{L}}|$ and $\hat{\mathbf{q}} = \hat{\mathbf{p}} \times \hat{\mathbf{n}}$. These are the principal axes for the wave; that is, they are defined so that the two polarizations are exactly 90° out of phase. The polarization basis tensors for these axes are $H_{ij}^+ = p_i p_j - q_i q_j$ and $H_{ij}^\times = p_i q_j + q_i p_j$:

$$h_{ij}(t) = h_+(t)H_{ij}^+ + h_\times(t)H_{ij}^\times, \quad (2.15)$$

where

$$h_+(t) = 2 \frac{\mathcal{M}^{5/3}(\pi f)^{2/3}}{D_L} [1 + (\hat{\mathbf{L}} \cdot \hat{\mathbf{n}})^2] \times \cos[\Phi(t) + \delta_p \Phi(t)], \quad (2.16)$$

$$h_\times(t) = -4 \frac{\mathcal{M}^{5/3}(\pi f)^{2/3}}{D_L} (\hat{\mathbf{L}} \cdot \hat{\mathbf{n}}) \sin[\Phi(t) + \delta_p \Phi(t)]. \quad (2.17)$$

These expressions were first discussed in the Introduction (albeit without the precessional phase correction). Here D_L is the luminosity distance to the source. Notice that the weighting of the two polarizations depends upon the direction of the angular momentum vector relative to the sky position.

We now consider the GW as measured by the detector. All of this analysis is done using the long wavelength ($\lambda \gg L$, where L is the LISA arm length) approximation introduced by Cutler [5]; more details can be found there. This approximation is appropriate for our purposes since most of the signal accumulates at low frequencies where the wavelength is in fact greater than the arm length. The full LISA response function, including arm-length effects, is discussed in [52,53].

LISA consists of three spacecraft arranged in an equilateral triangle, 5×10^6 km apart. The center of mass of the configuration orbits the sun 20° behind the Earth. The triangle is oriented at 60° to the ecliptic, so the orbits of the individual spacecraft will all be in different planes. This causes the triangle to spin around itself as it orbits the sun. Following Cutler, we define a barred “barycenter” coordinate system $(\bar{x}, \bar{y}, \bar{z})$, which is fixed in space with the $\bar{x} \bar{y}$ -plane aligned with the ecliptic, and an unbarred “detector” coordinate system (x, y, z) , which is attached to the detector. The z axis always points toward the sun, 60° away from vertical, while the x and y axes pinwheel around it. A particular binary will have fixed coordinates in the barycenter system, but its detector coordinates will be time varying.

The three arms act as a pair of two-arm detectors. We are first interested in the strain measured in detector I, that formed by arms 1 and 2:

$$h_1(t) = \frac{\delta L_1(t) - \delta L_2(t)}{L}, \quad (2.18)$$

where $\delta L_1(t)$ and $\delta L_2(t)$ are the differences in length in arms 1 and 2 as the wave passes. L is the unperturbed length of the arms. Using the geometry of the detector and the equation of geodesic deviation [54], we find

$$h_1(t) = \frac{\sqrt{3}}{2} \left[\frac{1}{2} (h_{xx} - h_{yy}) \right]. \quad (2.19)$$

To obtain h_{xx} and h_{yy} for use in these equations, we must rotate the waveform from the principal axes into the detector frame. The result is that detector I measures both polarizations, modulated by the antenna pattern of that detector:

$$h_1(t) = \frac{\sqrt{3}}{2} \frac{\mathcal{M}^{5/3}(\pi f)^{2/3}}{D_L} (2[1 + (\hat{\mathbf{L}} \cdot \hat{\mathbf{n}})^2] F_1^+(\theta_N, \phi_N, \psi_N) \times \cos[\Phi(t) + \delta_p \Phi(t)] - 4(\hat{\mathbf{L}} \cdot \hat{\mathbf{n}}) F_1^\times(\theta_N, \phi_N, \psi_N) \times \sin[\Phi(t) + \delta_p \Phi(t)]). \quad (2.20)$$

Detector I acts like a “standard” 90° GW interferometer (e.g. LIGO), with the response scaled by $\sqrt{3}/2$ (due to the 60° opening angle of the constellation). The antenna pattern functions are given by

$$F_1^+(\theta_N, \phi_N, \psi_N) = \frac{1}{2}(1 + \cos^2\theta_N) \cos 2\phi_N \cos 2\psi_N - \cos\theta_N \sin 2\phi_N \sin 2\psi_N, \quad (2.21)$$

$$F_1^\times(\theta_N, \phi_N, \psi_N) = \frac{1}{2}(1 + \cos^2\theta_N) \cos 2\phi_N \sin 2\psi_N + \cos\theta_N \sin 2\phi_N \cos 2\psi_N, \quad (2.22)$$

where θ_N and ϕ_N are the spherical angles for the binary's direction $\hat{\mathbf{n}}$ in the (unbarred) detector frame and ψ_N is the polarization angle of the wave in that frame:

$$\tan\psi_N = \frac{\hat{\mathbf{q}} \cdot \hat{\mathbf{z}}}{\hat{\mathbf{p}} \cdot \hat{\mathbf{z}}} = \frac{\hat{\mathbf{L}} \cdot \hat{\mathbf{z}} - (\hat{\mathbf{L}} \cdot \hat{\mathbf{n}})(\hat{\mathbf{z}} \cdot \hat{\mathbf{n}})}{\hat{\mathbf{n}} \cdot (\hat{\mathbf{L}} \times \hat{\mathbf{z}})}. \quad (2.23)$$

In order to use these expressions, we must relate the time-dependent angles in the unbarred detector frame, θ_N , ϕ_N , and ψ_N , to quantities in the barred barycenter frame. Again, the details can be found in Cutler [5].

Similar expressions hold for detector II. Following Cutler, we construct the signal from detector II as

$$h_{\text{II}}(t) = \frac{1}{\sqrt{3}}[h_1(t) + 2h_{\text{II}'}(t)], \quad (2.24)$$

where h_1 is the signal from detector I (2.18), and $h_{\text{II}'} = (\delta L_2(t) - \delta L_3(t))/L$ is the signal formed from the difference in the lengths of arms 2 and 3. This choice makes the noise in detector I uncorrelated with the noise in detector II; we will exploit this property in Sec. III to treat detectors I and II as independent detectors. From (2.24), we obtain

$$h_{\text{II}}(t) = \frac{\sqrt{3}}{2} \left[\frac{1}{2}(h_{xy} + h_{yx}) \right]. \quad (2.25)$$

The result is that detector II also behaves like a 90° interferometer (scaled by $\sqrt{3}/2$), but rotated by 45° with respect to detector I. Thus the antenna patterns for detector II are

$$F_{\text{II}}^+(\theta_N, \phi_N, \psi_N) = F_1^+(\theta_N, \phi_N - \pi/4, \psi_N), \quad (2.26)$$

$$F_{\text{II}}^\times(\theta_N, \phi_N, \psi_N) = F_1^\times(\theta_N, \phi_N - \pi/4, \psi_N). \quad (2.27)$$

We now rewrite the waveform in terms of an amplitude and phase. Letting $i = \text{I, II}$ label detector number, the waveform as measured by detector i is

$$h_i(t) = 2 \frac{\mathcal{M}^{5/3}(\pi f)^{2/3}}{D_L} A_{\text{pol},i}(t) \cos[\Phi(t) + \varphi_{\text{pol},i}(t) + \varphi_D(t) + \delta_p \Phi(t)], \quad (2.28)$$

where

$$A_{\text{pol},i}(t) = \frac{\sqrt{3}}{2} [(1 + (\hat{\mathbf{L}} \cdot \hat{\mathbf{n}})^2)^2 F_i^+(t)^2 + 4(\hat{\mathbf{L}} \cdot \hat{\mathbf{n}})^2 F_i^\times(t)^2]^{1/2} \quad (2.29)$$

is the ‘‘polarization amplitude’’ and

$$\varphi_{\text{pol},i}(t) = \tan^{-1} \left[\frac{2(\hat{\mathbf{L}} \cdot \hat{\mathbf{n}}) F_i^\times(t)}{[1 + (\hat{\mathbf{L}} \cdot \hat{\mathbf{n}})^2] F_i^+(t)} \right] \quad (2.30)$$

is the ‘‘polarization phase’’ [5]. We have introduced the ‘‘Doppler phase’’ $\varphi_D(t)$, which arises from the detector's motion around the sun and is given by

$$\varphi_D(t) = 2\pi f(t) R_\oplus \sin\bar{\theta}_N \cos[\bar{\Phi}_D(t) - \bar{\phi}_N], \quad (2.31)$$

where $\bar{\Phi}_D(t)$ is the orbital phase of the detector and $R_\oplus = 1$ AU.

Much of our analysis is done in the frequency domain. We define the Fourier transform of the signal as

$$\tilde{h}(f) = \int_{-\infty}^{\infty} e^{2\pi i f t} h(t) dt. \quad (2.32)$$

To evaluate the Fourier transform, we make use of the stationary phase approximation [8,9]. This approximation relies on the fact that the orbital time scale T_{orb} is much shorter than the precession time scale T_{prec} , as well as the inspiral time scale T_{insp} and detector orbital time scale $T_D = 1$ yr. The result thus differs from the true Fourier transform by terms of order $T_{\text{orb}}/T_{\text{prec}}$ and $T_{\text{orb}}/T_{\text{insp}}$ [29]. The Fourier transform is thus likely to be inaccurate near the end of the inspiral, when all of these time scales become comparable. Using (2.7) and (2.8), we have

$$\tilde{h}_i(f) = \sqrt{\frac{5}{96}} \frac{\pi^{-2/3} \mathcal{M}^{5/6}}{D_L} A_{\text{pol},i}[t(f)] f^{-7/6} e^{i(\Psi(f) - \varphi_{\text{pol},i}[t(f)] - \varphi_D[t(f)] - \delta_p \Phi[t(f)])}, \quad (2.33)$$

where the phase $\Psi(f)$ is given by

$$\Psi(f) = 2\pi f t_c - \Phi_c - \frac{\pi}{4} + \frac{3}{128} (\pi \mathcal{M} f)^{-5/3} \left[1 + \frac{20}{9} \left(\frac{743}{336} + \frac{11}{4} \eta \right) (\pi \mathcal{M} f)^{2/3} - 4(4\pi - \beta) (\pi \mathcal{M} f) + 10 \left(\frac{3\,058\,673}{1\,016\,064} + \frac{5429}{1008} \eta + \frac{617}{144} \eta^2 - \sigma \right) (\pi \mathcal{M} f)^{4/3} \right]. \quad (2.34)$$

In the work by Cutler [5], the separation of time scales that we used above leads to an interpretation of the polarization amplitude, polarization phase, and Doppler phase as mod-

ulations, in amplitude and phase, of an underlying carrier signal. These modulations make it possible to measure the sky position of the source, which also helps to measure the

luminosity distance D_L [6]. With the addition of precession, the polarization amplitude and polarization phase include additional modulations which further improve the measurement of these parameters. In conjunction with the purely intrinsic effects of precession, these effects also help us to better measure the masses and spins of the system.

III. MEASUREMENT AND PARAMETER ESTIMATION WITH LISA

A. Theory

In the previous section, we constructed the expected form for the GW strain that LISA is being designed to measure. The signal $s_i(t)$ as measured by detector i will of course also include noise $n_i(t)$:

$$s_i(t) = h_i(t) + n_i(t). \quad (3.1)$$

The LISA noise spectrum is discussed in Sec. III B; in this section, we discuss the theory of parameter estimation with a noisy signal. First, consider only one detector. We assume that the noise is zero mean, wide-sense stationary, and Gaussian. Wide-sense stationary means that the autocovariance function

$$K_n(t, t') = \langle n(t)n(t') \rangle - \langle n(t) \rangle \langle n(t') \rangle \quad (3.2)$$

depends only on the time difference $\tau = t - t'$. (Throughout this section, quantities within angle brackets are ensemble averaged with respect to the noise distribution.) A process is Gaussian if every sample of the process can be described as a Gaussian random variable and all possible sets of samples of the process are jointly Gaussian. However, the noise is colored, not white. A white noise process is defined to be a process which is uncorrelated with itself at different times; that is, its autocovariance is a delta function. Because the noise is colored, it has an interesting (nonflat) power spectral density (PSD), which is defined as the Fourier transform of the autocovariance function:

$$S_n(f) = 2 \int_{-\infty}^{\infty} d\tau e^{2\pi i f \tau} K_n(\tau). \quad (3.3)$$

The factor of 2 follows [8]; we actually use the *one-sided* PSD. Since the noise is Gaussian, it is described entirely by its second moments. Therefore, we will only need the PSD, and not the full probability density function, to analyze the effect of the noise on the signal.

Incidentally, it can be shown that wide-sense stationarity implies that the Fourier transform of $n(t)$ is a nonstationary white noise process in frequency:

$$\langle \tilde{n}(f)\tilde{n}^*(f') \rangle = \frac{1}{2}\delta(f - f')S_n(f). \quad (3.4)$$

The Fourier components are thus independent Gaussian random variables.

Now briefly consider both detectors. We explicitly constructed the second detector (2.24) [with $h(t) \rightarrow s(t)$] so

that the noise in it is uncorrelated with, and thus independent of, noise in the first detector. Thus we have

$$\langle \tilde{n}_i(f)\tilde{n}_j^*(f') \rangle = \frac{1}{2}\delta_{ij}\delta(f - f')S_n(f). \quad (3.5)$$

The uncorrelated nature of these two noises will allow us to easily generalize discussion from one detector to the full two effective detector system.

Let us write our generalized GW as $h(\boldsymbol{\theta})$, where the components of the vector $\boldsymbol{\theta}$ represent the various parameters on which the waveform depends. We now assume that a GW signal with particular parameters $\tilde{\boldsymbol{\theta}}$ is present in the data (i.e., “detection” has already occurred), and want to obtain estimates $\hat{\boldsymbol{\theta}}$ of those source parameters. Finn [28] shows that the probability for the noise to have some realization $n_0(t)$ is given by

$$p(n = n_0) \propto e^{-(n_0|n_0)/2}, \quad (3.6)$$

where the inner product used here is given by

$$(a|b) = 4 \operatorname{Re} \int_0^\infty df \frac{\tilde{a}^*(f)\tilde{b}(f)}{S_n(f)} \quad (3.7)$$

$$= 2 \int_0^\infty df \frac{\tilde{a}^*(f)\tilde{b}(f) + \tilde{a}(f)\tilde{b}^*(f)}{S_n(f)}. \quad (3.8)$$

This product is a natural one for the vector space of (frequency domain) signals $a(f)$. (Note that this definition of the inner product differs from [28] by a factor of 2.)

Given a particular measured signal $s(t)$, the probability that the GW parameters are given by $\tilde{\boldsymbol{\theta}}$ is the same as the probability that the noise takes the realization $s - h(\tilde{\boldsymbol{\theta}})$:

$$p(\tilde{\boldsymbol{\theta}}|s) \propto e^{-(h(\tilde{\boldsymbol{\theta}}) - s|h(\tilde{\boldsymbol{\theta}}) - s)/2}, \quad (3.9)$$

where the constant of proportionality may include prior probability densities for the parameters $\tilde{\boldsymbol{\theta}}$. For simplicity, we take these to be uniform.

We can estimate the parameters $\tilde{\boldsymbol{\theta}}$ by the maximum likelihood (ML) method. This method involves finding the parameters $\hat{\boldsymbol{\theta}}$ that maximize (3.9), or alternatively, minimize $(h(\tilde{\boldsymbol{\theta}}) - s|h(\tilde{\boldsymbol{\theta}}) - s)$, which can be considered a distance in signal space. A bank of template waveforms is correlated with the received signal and, assuming that any template produces a statistically significant correlation, the one with the highest correlation is the one with the ML parameters. The SNR for this signal is then given by [8]

$$\rho \approx (h(\hat{\boldsymbol{\theta}}|h(\hat{\boldsymbol{\theta}}))^{1/2} \approx (h(\tilde{\boldsymbol{\theta}}|h(\tilde{\boldsymbol{\theta}}))^{1/2}. \quad (3.10)$$

To quantify the errors in the ML estimate, we expand (3.9) around the most likely values $\hat{\boldsymbol{\theta}}$. We can then write the probability density as [8,9]:

$$p(\tilde{\boldsymbol{\theta}}|s) \propto e^{-\Gamma_{ab}\delta\theta^a\delta\theta^b/2}, \quad (3.11)$$

where $\delta\theta^a = \tilde{\theta}^a - \hat{\theta}^a$ and

$$\Gamma_{ab} = \left(\frac{\partial h}{\partial \theta^a} \middle| \frac{\partial h}{\partial \theta^b} \right), \quad (3.12)$$

evaluated at $\theta = \hat{\theta}$, is the Fisher information matrix. For small deviations from the ML estimate, the distribution is Gaussian. This expression holds for large values of the SNR (3.10). It is worth emphasizing at this point that, in our evaluation of Eq. (3.12), most derivatives are taken numerically using finite differencing—the complicated nature of the signal (due to the inclusion of spin precession) makes it essentially impossible to evaluate all but a few of our derivatives analytically. This is another reason that the code we have developed for this analysis is substantially slower than those developed for analyses which do not include spin-precession physics.

Now we return again to the two detector case. Using (3.5), we can write a total Fisher matrix as the sum of the individual Fisher matrices for each detector:

$$\Gamma_{ab}^{\text{tot}} = \Gamma_{ab}^{\text{I}} + \Gamma_{ab}^{\text{II}}. \quad (3.13)$$

The Fisher matrix is then inverted to produce the covariance matrix $\Sigma^{ab} = (\Gamma_{\text{tot}}^{-1})^{ab}$. The diagonal terms of the covariance matrix represent measurement errors:

$$\Delta \theta^a \equiv \sqrt{\langle (\delta \theta^a)^2 \rangle} = \sqrt{\Sigma^{aa}}. \quad (3.14)$$

The off-diagonal terms can be expressed as correlation coefficients, ranging from -1 to 1 :

$$c^{ab} \equiv \frac{\langle \delta \theta^a \delta \theta^b \rangle}{\Delta \theta^a \Delta \theta^b} = \frac{\Sigma^{ab}}{\sqrt{\Sigma^{aa} \Sigma^{bb}}}. \quad (3.15)$$

B. LISA detector and astrophysical noise

We turn now to a discussion of the noise we expect in LISA measurements. Our model for the instrumental noise spectrum, $S_h^{\text{inst}}(f)$, is based on that described in Ref. [55]. (From now on, we use the notation S_h for strain noise instead of S_n for general noise.) In particular, we use the online sensitivity curve generator provided by S. Larson, which implements the recipe of [55] (see [56]). The output of Larson’s webtool gives a sky averaged *amplitude* sensitivity curve, h_{Larson} . To convert to the noise we need for our analysis, we square this amplitude and insert two numerical factors:

$$S_h^{\text{inst}}(f) = \frac{1}{5} \times \left(\frac{\sqrt{3}}{2} h_{\text{Larson}} \right)^2 = \frac{3}{20} h_{\text{Larson}}^2. \quad (3.16)$$

The factor of $1/5$ accounts for the averaging of the antenna pattern functions over all sky positions and source orientations. This factor is only correct for measuring radiation with wavelength $\lambda \gg L$ (where L is the LISA arm length). As a consequence, our instrumental noise will be inaccurate at high frequencies. This will have little impact on our analysis since, as already argued, the signal from merging binary black holes accumulates at low frequencies.

The factor $\sqrt{3}/2$ arises due to the 60° opening angle of the interferometer arms; we have already accounted for this factor in our discussion of the interferometer’s interaction with a GW [cf. Eqs. (2.19) and (2.25)]. The numerical factor $3/20$ has been the source of some confusion; Berti, Buonanno, and Will very nicely straightened this out. See Sec. IIC of Ref. [7] for further discussion of these factors.

Besides purely instrumental noise, LISA data will contain “noise” from a background of confused binary sources,⁸ mostly white dwarf binaries. An isotropic background of indistinguishable sources can be represented as noise with spectral density [27]

$$S_h^{\text{conf}}(f) = \frac{3}{5\pi} f^{-3} \rho_c \Omega_{\text{GW}}(f), \quad (3.17)$$

where $\rho_c = 3H_0^2/8\pi$ is the critical energy density to close the universe and $\Omega_{\text{GW}} = (f/\rho_c) d\rho_{\text{GW}}/df$ is the energy density in GWs relative to ρ_c per logarithmic frequency interval. Using this form and the results of Farmer and Phinney [57], we model the confusion noise due to extragalactic binary sources by

$$S_h^{\text{exgal}}(f) = 4.2 \times 10^{-47} \left(\frac{f}{1 \text{ Hz}} \right)^{-7/3} \text{ Hz}^{-1}. \quad (3.18)$$

From Nelemans *et al.* [58], we take the galactic white dwarf confusion noise to be

$$S_h^{\text{gal}}(f) = 2.1 \times 10^{-45} \left(\frac{f}{1 \text{ Hz}} \right)^{-7/3} \text{ Hz}^{-1}. \quad (3.19)$$

The combined instrumental and galactic confusion noise is given by [27]

$$S_h^{\text{inst+gal}}(f) = \min[S_h^{\text{inst}}(f) / \exp(-\kappa T_{\text{mission}}^{-1} dN/df), S_h^{\text{inst}}(f) + S_h^{\text{gal}}(f)]. \quad (3.20)$$

The choice taken in Eq. (3.20) reflects the fact that, at sufficiently high frequency, the number of binaries per bin should be small enough that they are no longer truly confused and can be subtracted from the data stream (at least partially). The factor $\exp(-\kappa T_{\text{mission}}^{-1} dN/df)$ is the fraction of “uncorrupted” frequency bins. We choose $\kappa = 4.5$ [59], T_{mission} is the mission duration (which we take to be three years), and

$$\frac{dN}{df} = 2 \times 10^{-3} \left(\frac{1 \text{ Hz}}{f} \right)^{11/3} \text{ Hz}^{-1} \quad (3.21)$$

is the number density of galactic binaries per unit frequency [6].

⁸While surely noise when studying cosmological black holes, this background is *signal* to those interested in stellar populations.

Finally, the total noise is given by

$$S_h(f) = S_h^{\text{inst+gal}}(f) + S_h^{\text{exgal}}(f). \quad (3.22)$$

IV. RESULTS

A. Procedure

1. Parameter space

Seventeen parameters describe the most general binary black hole inspiral waveform [26]. Two of these are the orbital eccentricity and the orientation of the orbital ellipse; since we only consider circular orbits, we can ignore these two. The other 15 parameters are all necessary to describe the full post-Newtonian waveform with precession effects that we described in Sec. II.

We divide this set into intrinsic and extrinsic parameters. In our labeling system, intrinsic parameters are those which label properties intrinsic to the binary itself; extrinsic parameters label properties which depend upon the position and placement of the binary relative to the observer. One can regard intrinsic parameters as describing the physics or astrophysics of the binary system, and extrinsic parameters as describing the binary's astronomical properties.

The intrinsic parameters we use are $\ln m_1$; $\ln m_2$; $\bar{\mu}_L(0) \equiv \cos[\bar{\theta}_L(0)]$ and $\bar{\phi}_L(0)$, the initial direction of the orbital angular momentum; $\bar{\mu}_{S_1}(0) \equiv \cos[\bar{\theta}_{S_1}(0)]$, $\bar{\phi}_{S_1}(0)$, $\bar{\mu}_{S_2}(0) \equiv \cos[\bar{\theta}_{S_2}(0)]$, and $\bar{\phi}_{S_2}(0)$, the initial directions of the spins; χ_1 and χ_2 , the dimensionless spin parameters; t_c , the time at coalescence; and Φ_c , the phase at coalescence. (Note that t_c and Φ_c could very well be considered extrinsic in our labeling system, since they just label the system's state at some particular time. At any rate, neither t_c nor Φ_c is of much physical interest, so their categorization is not too important.) Our extrinsic parameters are $\bar{\mu}_N = \cos\bar{\theta}_N$ and $\bar{\phi}_N$, the sky position in barycenter coordinates; and $\ln D_L$, the luminosity distance to the binary. All of these parameters must be fit in a measurement and thus must be included in our Fisher matrix analysis. We are not necessarily interested in all of them, however. In particular, we will focus on the masses, the dimensionless spin parameters, the sky position, and the luminosity distance.

It is worth noting that this choice of parameters is not the same as that used in analyses which neglect precession. In that case, the direction of the angular momentum $\hat{\mathbf{L}}$ is constant, and so the system's orientation is constant and fully described using two angles (e.g., $\bar{\mu}_L$ and $\bar{\phi}_L$). Including precession, $\hat{\mathbf{L}}$ is no longer constant, but evolves according to (2.11). The solution to this differential equation requires two initial conditions, for instance, $\bar{\mu}_L(0)$ and $\bar{\phi}_L(0)$, which can be used as parameters of the system. Since these initial conditions are taken at the (somewhat arbitrary) starting point of our calculations, they do not hold much physical interest (though they must be fit for and thus included in our Fisher matrix).

Previous analyses, including the precursor to this work [6], have used β (2.5) and σ (2.6) as parameters—these are constants when precession is neglected. They are also the only combinations of the spin magnitudes and spin angles that enter into the expression for the waveform. Boiling the six numbers which characterize \mathbf{S}_1 and \mathbf{S}_2 down to two greatly simplifies the parameter space, but also restricts us from being able to measure, for example, the black holes' spin magnitudes. When precession is included, β and σ are no longer constants. In addition, they no longer fully characterize the signal, since the precession equations (2.9), (2.10), and (2.11) depend on all of the components of the spins. We thus need six spin-related parameters to fully describe the signal: the magnitudes of the spins and their orientations at some initial time. The orientations are again uninteresting, but the fact that we can measure the magnitudes of the spins and quantify their errors is quite interesting and new to this analysis.

Finally, we break from tradition and use $\ln m_1$ and $\ln m_2$ to parametrize our masses rather than $\ln \mathcal{M}$ and $\ln \mu$. The chirp mass and reduced mass have been used in most previous work because of their appearance in the waveform phase $\Psi(f)$. However, the precession equations, as well as the spin parameters β and σ , depend on the individual masses of the black holes. It is a simple matter in principle to just solve for $m_{1,2}(\mathcal{M}, \mu)$ and substitute into the precession equations. Unfortunately, the Jacobian of the transformation between (\mathcal{M}, μ) and (m_1, m_2) is singular when $m_1 = m_2$, leading to problems in evaluating the Fisher matrix.

These problems can be illustrated analytically. Consider how derivatives of some function $f(m_1, m_2)$ with respect to \mathcal{M} behave:

$$\frac{\partial f}{\partial \mathcal{M}} = \sum_{i=1}^2 \frac{\partial f(m_1, m_2)}{\partial m_i} \frac{\partial m_i(\mathcal{M}, \mu)}{\partial \mathcal{M}}. \quad (4.1)$$

When $m_1 = m_2$, the final derivative diverges—a behavior that we have seen numerically. The Fisher information is infinite, and the Gaussian approximation breaks down; the same problem occurs for μ . Thus, we argue that, when precession is included, \mathcal{M} and μ are no longer a good choice of parameters to describe the system. Since we are still interested in the errors in $\ln \mathcal{M}$ and $\ln \mu$ (which are determined to higher accuracy than the individual masses), we convert using the propagation of errors formulas

$$\begin{aligned} \left(\frac{\Delta \mathcal{M}}{\mathcal{M}}\right)^2 &= \left(\frac{m_1}{\mathcal{M}}\right)^2 \left(\frac{\partial \mathcal{M}}{\partial m_1}\right)^2 \left(\frac{\Delta m_1}{m_1}\right)^2 \\ &+ \left(\frac{m_2}{\mathcal{M}}\right)^2 \left(\frac{\partial \mathcal{M}}{\partial m_2}\right)^2 \left(\frac{\Delta m_2}{m_2}\right)^2 \\ &+ \left(\frac{m_1 m_2}{\mathcal{M}^2}\right) \left(\frac{\partial \mathcal{M}}{\partial m_1}\right) \left(\frac{\partial \mathcal{M}}{\partial m_2}\right) \Sigma^{\ln m_1, \ln m_2}, \end{aligned} \quad (4.2)$$

$$\begin{aligned} \left(\frac{\Delta\mu}{\mu}\right)^2 &= \left(\frac{m_1}{\mu}\right)^2 \left(\frac{\partial\mu}{\partial m_1}\right)^2 \left(\frac{\Delta m_1}{m_1}\right)^2 + \left(\frac{m_2}{\mu}\right)^2 \left(\frac{\partial\mu}{\partial m_2}\right)^2 \left(\frac{\Delta m_2}{m_2}\right)^2 \\ &+ \left(\frac{m_1 m_2}{\mu^2}\right) \left(\frac{\partial\mu}{\partial m_1}\right) \left(\frac{\partial\mu}{\partial m_2}\right) \Sigma^{\ln m_1, \ln m_2}. \end{aligned} \quad (4.3)$$

For unequal masses, we find that computing errors in m_1 and m_2 and then converting gives the same result as simply computing errors in \mathcal{M} and μ directly. We do not find good agreement in the equal mass case; for the reasons discussed above, however, we do not trust the (\mathcal{M}, μ) parametrization in this case. At any rate, the case $m_1 = m_2$ is quite implausible in nature, so this is almost certainly a moot point as far as real measurements are concerned.⁹ We note that Vecchio [26], for simplicity, considers the equal mass case exclusively but does not report any anomalous behavior such as we have seen. We are puzzled about this discrepancy.

2. Calculations

The code we use to calculate parameter measurement errors is based on that used in [6]. It is written in C++ using several routines taken, sometimes with slight modification, from [60]. As in [6], we perform Monte Carlo simulations in which we specify rest-frame masses and redshift and then randomly choose sky position, initial angular momentum and spin directions, spin magnitudes, and time of coalescence within the three-year LISA mission window. We specify spin magnitudes for some studies as well.

The primary function of the code is the calculation of the full gravitational waveform, including precessional effects. In order to effectively use the formulas of Sec. III, we take the wave frequency f as the independent variable. The elapsed time is related to the frequency using (2.7). The calculation is started when the waveform enters LISA's band (taken to be $f_{\min} = 3 \times 10^{-5}$ Hz throughout this paper) or when the LISA mission begins, whichever is later. (By treating the time of coalescence as a Monte Carlo variable, some signals will be partially cut off because they are already in band when LISA begins observations.) The calculation proceeds until the binary reaches the Schwarzschild innermost stable circular orbit (ISCO) at orbital separation $r = 6M$. Though perhaps a somewhat crude choice, we use this criterion for simplicity. Choosing slightly different cutoff radii does not change our results very much; at any rate, the post-Newtonian phase formula and precession equations we use in this regime are unlikely to be very accurate. The frequency at this point, which we call the “merge frequency,” can be found using (2.1) for $r = 6M$ (plus $f = \Omega/\pi$). Note that f depends on the directions of the angular momentum and spin vectors as a function of time; since we have not found them yet, this value can only be an estimate of where to stop. Any

⁹It is worth noting that even a slight mass difference (a few percent) is sufficient for the two approaches to match.

error due to this approximation is no doubt unimportant compared to the arbitrary selection of $r = 6M$ for the transition.

Once the frequency range has been determined, the true work begins. We integrate the precession equations (2.9), (2.10), and (2.11) using a Runge-Kutta routine to find the values of $\hat{\mathbf{L}}$, $\hat{\mathbf{S}}_1$, and $\hat{\mathbf{S}}_2$ over the duration of the signal. The routine is a fifth-order adaptive step algorithm in the frequency domain. At each frequency, the code takes the results for the three orbital angular momentum components and six spin components and uses them to calculate $\bar{\mu}_L$, $\bar{\phi}_L$, β , and σ . It also computes the integrated correction to the phase using the derivative (2.14).

As already discussed, our derivatives are taken numerically rather than analytically. We therefore must do the integration described above a total of 21 times: once for the given values of the parameters, and twice more for small shifts in each parameter which requires a numerical derivative. This repetition slows the code quite drastically compared to its earlier incarnation—an unfortunate but unavoidable cost.

Once all of the necessary integrations are complete, the SNR (3.10) and the Fisher matrix (3.12) can be calculated for each of the two effective detectors of LISA using the noise $S_h(f)$ (see Sec. III B). Some previous work [5,7] investigated parameter estimation using the signal from only one synthesized detector; we will always assume that both are operational. It would be interesting to see how measurement degradation due to only having a single operating detector can be ameliorated by including precession effects.

At this stage, the necessary integrals are performed using Curtis-Clenshaw quadrature, which depends on the decomposition of the integrand into Chebyshev polynomials [60]. This method keeps the code reasonably fast even with the addition of the Runge-Kutta routine. At each step of the integration, the integrator uses the values that were calculated using that Runge-Kutta routine to evaluate the waveform and/or its appropriate derivatives. The derivatives are calculated using

$$\frac{df}{d\theta} \approx \frac{f(\theta + \frac{\Delta\theta}{2}) - f(\theta - \frac{\Delta\theta}{2})}{\Delta\theta}. \quad (4.4)$$

For all parameters, we use $\Delta\theta = 10^{-5}\theta$. We invert the Fisher matrix using LU decomposition to produce the covariance matrix [60]. In “poor” cases (e.g., high mass binaries at large redshift), the Fisher matrix can be nearly singular, with a large condition number.¹⁰ In such a case, the covariance matrix produced by the code may not be the true inverse of the Fisher matrix (and may not even be

¹⁰The “condition number” is the ratio of the largest eigenvalue of a matrix to the smallest. A rule of thumb is that matrix inversion breaks down when the logarithm of the condition number of a matrix exceeds the number of digits of accuracy in the matrix elements (see, e.g., discussion in [60]).

positive definite). This problem is largely ameliorated by representing our numerical data in long double format—this improves (relative to type double) matrix inverses in many “bad” cases but leaves all other cases essentially unchanged.

It is worth noting that the bad cases are typically ones in which the binary executes very few orbits over the course of the measurement. We are confident in our results for all cases in which the number of measured orbits, $N_{\text{orb}} = \Phi_{\text{orb}}/2\pi$, is greater than ~ 10 – 20 . When the number of orbits is small (and the condition number is concomitantly high), the errors are so large that they are basically meaningless. In such a case, measurement would not determine the system’s characteristics in any meaningful sense.

B. Black hole masses and spins

Representative examples of our results are shown in Figs. 2 and 3. These histograms show the spread of errors in \mathcal{M} and μ for a sample of 10^4 binaries at $z = 1$ with rest-frame masses $m_1 = 10^6 M_\odot$ and $m_2 = 3 \times 10^5 M_\odot$. Each figure compares the results of the new code to those of the original code of [6], which neglects precession. (This code has been updated to reflect up-to-date models for LISA noise; some minor coding errors have also been corrected.) Clearly, including spin precession leads to a significant improvement in the measurement of these mass parameters. The reduced mass μ , in particular, is improved. This is because the time variation of β and σ breaks a near degeneracy between those terms and μ in the post-Newtonian phase (2.34). The masses also control the precession rate, as seen in (2.9), (2.10), and (2.11). (Recall that, in those equations, $S_i = \chi_i m_i^2$.) This means that they

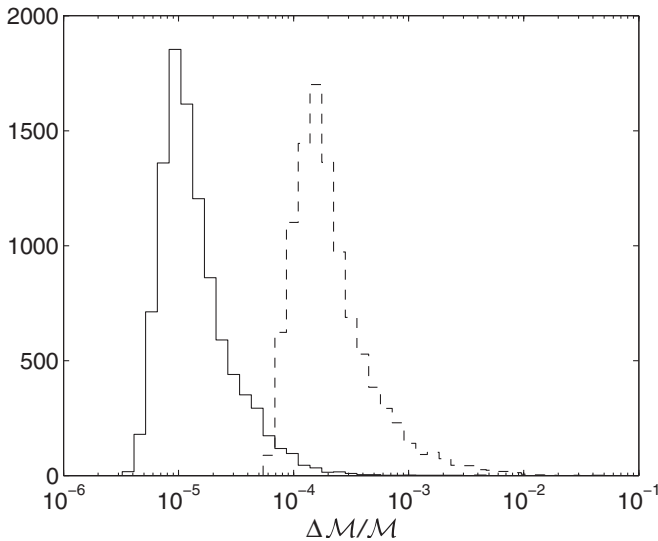


FIG. 2. Distribution of errors in chirp mass \mathcal{M} for 10^4 binaries with $m_1 = 10^6 M_\odot$ and $m_2 = 3 \times 10^5 M_\odot$ at $z = 1$. The dashed line is the precession-free calculation; the solid line includes precession. Precession reduces the measurement error by about an order of magnitude.

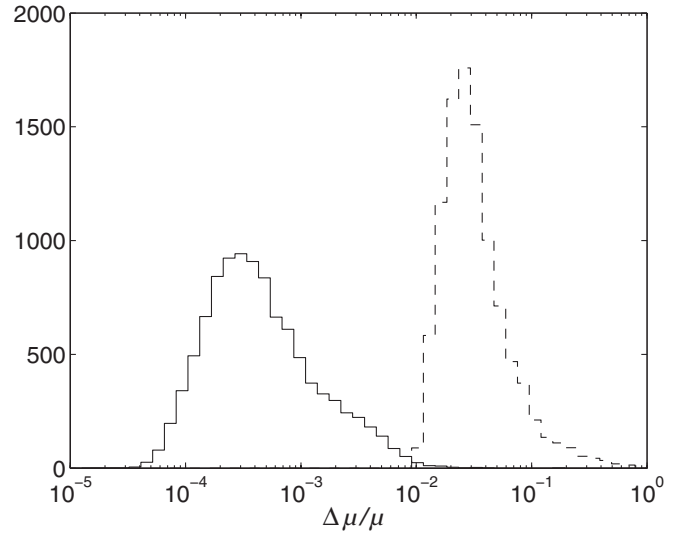


FIG. 3. Distribution of errors in reduced mass μ for 10^4 binaries with $m_1 = 10^6 M_\odot$ and $m_2 = 3 \times 10^5 M_\odot$ at $z = 1$. The dashed line is the precession-free calculation; the solid line includes precession. Precession has an enormous effect on the reduced mass, which was previously highly correlated with the parameters β and σ .

now influence the polarization amplitude and polarization phase; they do not influence those quantities when precession is neglected. These precession-induced influences on the waveform make it possible to determine the masses even more accurately than before.

As discussed earlier, we have found the masses m_1 and m_2 to be more useful parameters than \mathcal{M} and μ when precession is included. Figure 4 shows the error in mea-

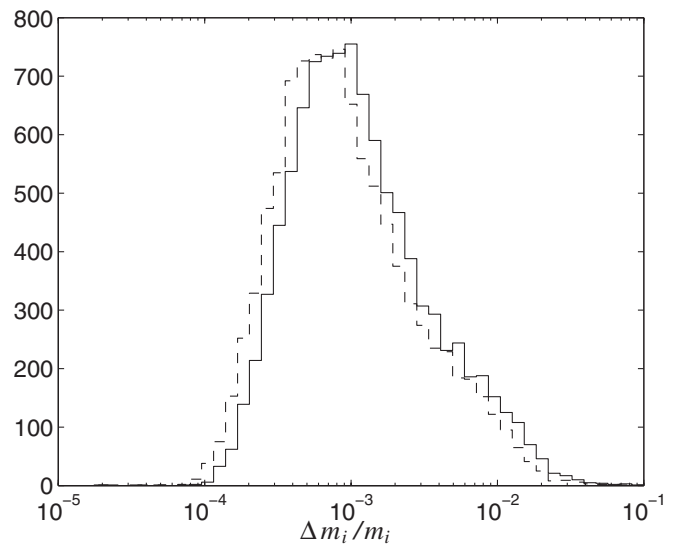


FIG. 4. Distribution of errors in individual hole masses for 10^4 binaries at $z = 1$. The solid line is $m_1 = 10^6 M_\odot$, while the dashed line is $m_2 = 3 \times 10^5 M_\odot$. The individual masses are not determined as well as \mathcal{M} and μ , but they are better behaved parameters when precession is introduced.

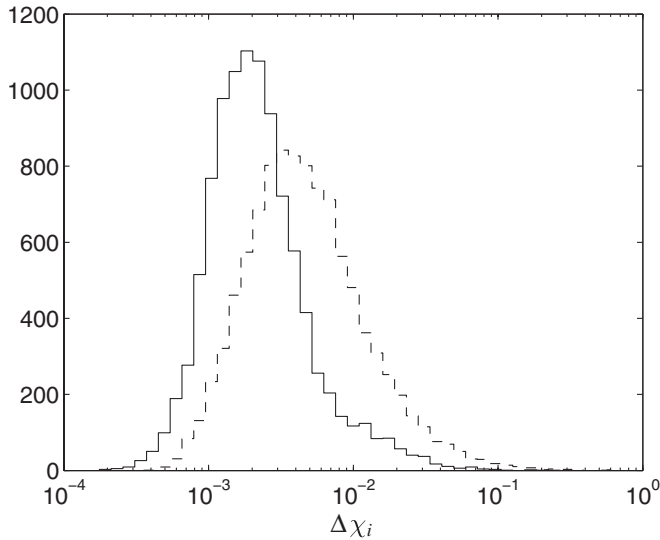


FIG. 5. Distribution of errors in dimensionless spin parameters χ_1 (solid line) and χ_2 (dashed line) for 10^4 binaries with $m_1 = 10^6 M_\odot$ and $m_2 = 3 \times 10^5 M_\odot$ at $z = 1$. In each binary, the spin values are randomly selected between 0 and 1. The higher mass then has, on average, higher total spin and more effect on the precession.

measurements of the individual masses for our example system. While these masses are measured quite accurately, they are not measured as accurately as \mathcal{M} and μ . This reflects the fact that, even though the individual masses play a role in the precession, the other parts of the waveform depend explicitly on the combinations \mathcal{M} and μ . Notice also that the smaller mass is typically determined a bit better than the larger one, though the difference is not large.

Precession makes it possible to determine the spins of the binary's members. Figure 5 shows the error in measurements of the two dimensionless spin parameters χ_1 and χ_2 . We see that χ is generally determined very well: Taking a typical spin parameter to be about 0.5 (recall we randomly choose χ between 0 and 1), the bulk of this distribution corresponds to errors of a bit less than a percent. For this entirely random distribution of χ , the dimensionless spin parameter of the larger hole tends to be better determined than that of the smaller hole. This appears to be a simple consequence of the fact that black hole spin scales as mass squared ($S_i = \chi_i m_i^2$), and larger spin has more of an impact on the waveform.

Next, we examine how well spin is measured as a function of spin magnitude. Figure 6 shows the error in χ_1 for the same system as in Fig. 5, except that we set $\chi_1 = \chi_2 = 0.9$ (solid line) and $\chi_1 = \chi_2 = 0.1$ (dashed line), rather than randomly distributing their values. This allows us to more accurately assess how well spin is determined as a function of its value, as well as to more accurately determine the percent error we expect in these measurements. For $\chi_1 = \chi_2 = 0.1$, the error is almost 10%, while

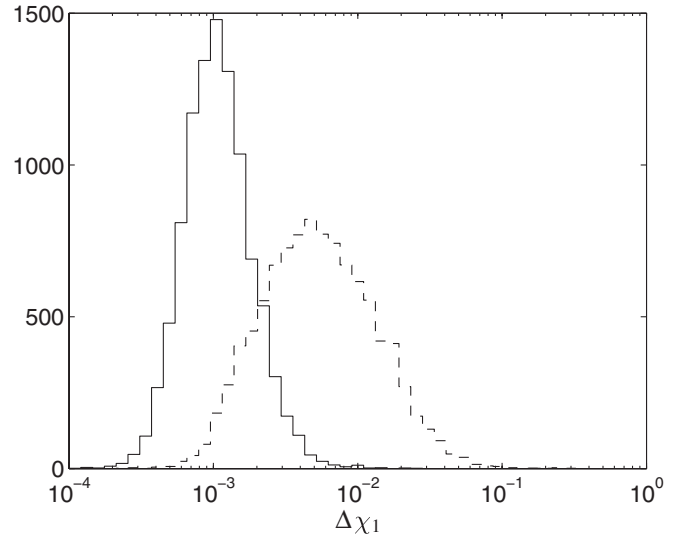


FIG. 6. Distribution of errors in dimensionless spin parameter χ_1 for 10^4 binaries with $m_1 = 10^6 M_\odot$ and $m_2 = 3 \times 10^5 M_\odot$ at $z = 1$. Here, spin magnitudes have been set to a specified value—low spin, $\chi_1 = \chi_2 = 0.1$ (dashed line), and high spin, $\chi_1 = \chi_2 = 0.9$ (solid line). Since greater spin more strongly impacts the waveform, the high spin case is measured more accurately.

for $\chi_1 = \chi_2 = 0.9$, the error is closer to 0.1%. This is a considerable difference and is easily ascribed to the fact that rapid spin has a much stronger impact on the waveform.

Table I shows the median errors in intrinsic parameters for different mass ratios at $z = 1$. We continue to include the errors in \mathcal{M} and μ for comparison with the precession-free case, but only in binaries of unequal mass where the Gaussian approximation is well defined. Examining the table, we see some interesting features. The errors, in general, are worse for higher mass binaries, which spend less time in the LISA band. At $m_1 = m_2 = 10^7 M_\odot$, the mass errors jump to nearly 10%, compared to tenths of a percent at the next lower mass combination. In addition, the spin determination becomes very unreliable. Mass ratio also has an important effect on the results. Taking into account the general trend caused by total mass, we see that unequal mass ratios generally produce better results. This is good news for eventual measurements of astrophysical systems, since merger tree calculations show that binaries are most likely to have mass ratios of about 10 [51]. To understand the mass ratio dependence, we again turn to the precession equations (2.9), (2.10), and (2.11). For unequal mass ratios, the geodetic spin-orbit and spin-spin terms will cause the two spins to precess at different rates, creating richer features in the signal than for equal mass ratios. This illustrates the importance of effects beyond the “simple precession” of [26,29]. We also see that the trends of Figs. 4 and 5 hold for each unequal mass binary in the table. That is, the mass of the smaller hole is determined

TABLE I. Median errors in intrinsic quantities for 10^4 binaries of various masses at $z = 1$, including comparisons with the “no precession” case where possible. We have omitted the errors in chirp mass and reduced mass for equal mass binaries because that parametrization of the waveform fails the Gaussian approximation at those points.

$m_1(M_\odot)$	$m_2(M_\odot)$	$\Delta m_1/m_1$	$\Delta m_2/m_2$	$\Delta\chi_1$	$\Delta\chi_2$	$\Delta\mathcal{M}/\mathcal{M}$ (no precession)	$\Delta\mathcal{M}/\mathcal{M}$ (precession)	$\Delta\mu/\mu$ (no precession)	$\Delta\mu/\mu$ (precession)
10^5	10^5	0.000 629	0.000 629	0.003 60	0.003 55
3×10^5	10^5	0.000 584	0.000 475	0.001 16	0.002 62	6.15×10^{-5}	5.33×10^{-6}	0.0119	0.000 210
3×10^5	3×10^5	0.000 890	0.000 888	0.004 79	0.004 68
10^6	10^5	0.000 557	0.000 393	0.000 791	0.004 28	0.000 161	1.12×10^{-5}	0.0187	0.000 307
10^6	3×10^5	0.000 998	0.000 796	0.002 00	0.004 29	0.000 177	1.19×10^{-5}	0.0285	0.000 383
10^6	10^6	0.001 61	0.001 61	0.008 04	0.007 78
3×10^6	3×10^5	0.000 819	0.000 580	0.000 965	0.005 29	0.000 606	2.53×10^{-5}	0.0572	0.000 454
3×10^6	10^6	0.002 04	0.001 65	0.002 79	0.005 57	0.001 31	4.52×10^{-5}	0.149	0.000 732
3×10^6	3×10^6	0.005 13	0.005 14	0.0250	0.0254
10^7	10^6	0.002 09	0.001 60	0.001 95	0.0152	0.008 26	0.000 238	0.496	0.001 27
10^7	3×10^6	0.007 43	0.006 05	0.007 17	0.0163	0.008 82	0.000 630	0.614	0.003 01
10^7	10^7	0.0903	0.0886	0.542	0.542

better than the mass of the larger hole, but the spin of the larger hole is determined better than the spin of the smaller hole.

Tables II and III show the same results for $z = 3$ and $z = 5$, respectively. The trends we see at $z = 1$ largely continue at these redshifts. In general, the errors get worse at higher redshift as the signal amplitude degrades and more of the signal is redshifted out of band. It is worth noting that the change is generally greater from $z = 1$ to $z = 3$ than from $z = 3$ to $z = 5$. This effect was also seen by Berti, Buonanno, and Will [7] and can be explained by considering the redshift dependence of the wave amplitude. Neglecting all the angular factors and remembering to redshift quantities with the dimensions of time, we find that the amplitude scales like $(1+z)/D_L(z) = 1/D_M(z)$, where $D_M(z)$ is the proper motion distance. This distance measure varies more strongly with z at low redshift than at high redshift. (See [61] for a plot of $D_M(z)$.) Consequently,

when moving from $z = 1$ to $z = 3$, the amplitude, and thus the SNR, decreases more than when moving from $z = 3$ to $z = 5$. For lower mass binaries, this amplitude decrease plays a bigger role in the loss of SNR than does redshifting the spectrum to a lower frequency; most of the SNR is accumulated late in the inspiral, where the orbits are in a relatively flat region of the sensitivity curve.

By contrast, for the highest mass binaries, redshifting of the spectrum can have a dramatic effect. So much of their signal is moved out of band that LISA may measure their waves for only a very short time. As such, measurement may not provide sufficient information to constrain 15 parameters. This is reflected in the high condition numbers associated with such cases. Their Fisher matrices are thus nearly singular, and their inverses are untrustworthy. In fact, measurement error in these binaries actually *degrades* when precession is included. The time in band is too short for precession effects to accumulate. They do not aid

 TABLE II. Median errors in intrinsic quantities for 10^4 binaries of various masses at $z = 3$.

$m_1(M_\odot)$	$m_2(M_\odot)$	$\Delta m_1/m_1$	$\Delta m_2/m_2$	$\Delta\chi_1$	$\Delta\chi_2$	$\Delta\mathcal{M}/\mathcal{M}$ (no precession)	$\Delta\mathcal{M}/\mathcal{M}$ (precession)	$\Delta\mu/\mu$ (no precession)	$\Delta\mu/\mu$ (precession)
10^5	10^5	0.002 95	0.002 95	0.0165	0.0160
3×10^5	10^5	0.003 23	0.002 62	0.006 68	0.0144	0.000 422	3.27×10^{-5}	0.0742	0.001 16
3×10^5	3×10^5	0.004 76	0.004 74	0.0245	0.0240
10^6	10^5	0.002 74	0.001 93	0.003 53	0.0188	0.001 24	6.75×10^{-5}	0.133	0.001 51
10^6	3×10^5	0.005 51	0.004 41	0.008 79	0.0187	0.001 82	9.42×10^{-5}	0.238	0.002 12
10^6	10^6	0.0120	0.0120	0.0576	0.0568
3×10^6	3×10^5	0.004 84	0.003 46	0.004 82	0.0299	0.006 83	0.000 283	0.485	0.002 71
3×10^6	10^6	0.0160	0.0131	0.0174	0.0342	0.007 46	0.000 675	0.606	0.005 85
3×10^6	3×10^6	0.0690	0.0678	0.402	0.404
10^7	10^6	0.0250	0.0287	0.0359	0.333	0.0195	0.009 51	0.690	0.0243
10^7	3×10^6	0.437	0.346	0.327	0.619	0.0192	0.0704	0.646	0.177
10^7	10^7	21.6	21.2	104	104

TABLE III. Median errors in intrinsic quantities for 10^4 binaries of various masses at $z = 5$. The results for the highest masses are meaningless—the parameters are completely undetermined.

$m_1(M_\odot)$	$m_2(M_\odot)$	$\Delta m_1/m_1$	$\Delta m_2/m_2$	$\Delta \chi_1$	$\Delta \chi_2$	$\Delta \mathcal{M}/\mathcal{M}$ (no precession)	$\Delta \mathcal{M}/\mathcal{M}$ (precession)	$\Delta \mu/\mu$ (no precession)	$\Delta \mu/\mu$ (precession)
10^5	10^5	0.006 46	0.006 45	0.0348	0.0340
3×10^5	10^5	0.007 35	0.005 97	0.0151	0.0312	0.001 07	8.06×10^{-5}	0.178	0.002 64
3×10^5	3×10^5	0.0109	0.0109	0.0542	0.0527
10^6	10^5	0.005 95	0.004 21	0.007 01	0.0384	0.003 36	0.000 184	0.313	0.003 30
10^6	3×10^5	0.0133	0.0107	0.0183	0.0387	0.004 58	0.000 309	0.491	0.005 16
10^6	10^6	0.0373	0.0374	0.181	0.184
3×10^6	3×10^5	0.0141	0.0105	0.0130	0.0961	0.0122	0.001 35	0.652	0.008 30
3×10^6	10^6	0.0517	0.0426	0.0515	0.105	0.0113	0.003 74	0.635	0.0193
3×10^6	3×10^6	0.422	0.419	2.60	2.60
10^7	10^6	0.260	0.315	0.387	3.41	0.0416	0.137	0.713	0.273
10^7	3×10^6	15.5	11.5	10.1	16.4	0.120	2.75	0.797	5.97
10^7	10^7	57 400	57 100	262 000	261 000

parameter estimation; instead, the need to fit extra parameters causes errors to be worse.

C. Sky position and distance to source

We now focus on extrinsic parameters, the sky position and the luminosity distance to the source. We find that the determination of these parameters is likewise improved when precession physics is taken into account, though not as strongly as for intrinsic parameters. This might be expected, since precession is an intrinsic effect local to the binary and has no direct dependence on these extrinsic parameters. Precession's impact on the extrinsic parameters is somewhat more indirect—it largely improves their determination by reducing the (otherwise quite strong) correlation between sky position and the orbital angular momentum direction $\hat{\mathbf{L}}$ and between these angles and the source's luminosity distance.

In our analysis, a binary's position on the sky is characterized by the two parameters $\boldsymbol{\theta} = (\bar{\mu}_N = \cos \bar{\theta}_N, \bar{\phi}_N)$. Consider the subspace containing just these two parameters. The Fisher matrix is a 2×2 matrix which characterizes the probability density for the true parameters given a measured signal [see (3.11)]:

$$p(\bar{\boldsymbol{\theta}}|s) \propto \exp(-\frac{1}{2}\Gamma_{ab}\delta\theta^a\delta\theta^b). \quad (4.5)$$

To accurately describe the error ellipse on the sky, we need to manipulate the right-hand side of (4.5) in several ways. First, we change coordinates from $\bar{\mu}_N$ to $\bar{\theta}_N$, while leaving $\bar{\phi}_N$ alone; schematically, we can represent this as $\theta^a \rightarrow \theta^{a'}$. This transformation gives $\delta\bar{\theta}_N = (d\bar{\theta}_N/d\bar{\mu}_N)\delta\bar{\mu}_N = -\delta\bar{\mu}_N/\sin\bar{\theta}_N$.

Next, we need to redefine what we mean by “error” in order to make the results more relevant to observations. To do so, we define the “proper” angular errors $\delta\bar{\theta}_N^p = \delta\bar{\theta}_N$ and $\delta\bar{\phi}_N^p = \sin\bar{\theta}_N\delta\bar{\phi}_N$. The proper angular errors are just the normal coordinate errors rescaled by the metric of the

sphere to correctly account for the proper size of a segment $\delta\bar{\phi}_N$ at different $\bar{\theta}_N$. Substituting all of these changes into (4.5), we obtain

$$p(\bar{\boldsymbol{\theta}}|s) \propto \exp(-\frac{1}{2}\Gamma_{a'b'}^p\delta\theta_p^{a'}\delta\theta_p^{b'}), \quad (4.6)$$

where we have defined a proper Fisher matrix for the parameters $(\bar{\theta}_N, \bar{\phi}_N)$. In terms of the original Fisher matrix, the elements are

$$\Gamma_{\bar{\theta}_N\bar{\theta}_N}^p = \sin^2\bar{\theta}_N\Gamma_{\bar{\mu}_N\bar{\mu}_N}, \quad (4.7)$$

$$\Gamma_{\bar{\theta}_N\bar{\phi}_N}^p = \Gamma_{\bar{\phi}_N\bar{\theta}_N}^p = -\Gamma_{\bar{\mu}_N\bar{\phi}_N}, \quad (4.8)$$

$$\Gamma_{\bar{\phi}_N\bar{\phi}_N}^p = \csc^2\bar{\theta}_N\Gamma_{\bar{\phi}_N\bar{\phi}_N}. \quad (4.9)$$

Finally, we diagonalize the Fisher matrix by rotating our parametrization, $\theta^{a'} \rightarrow \theta^{\hat{a}}$, such that the probability (4.6) becomes

$$p(\bar{\boldsymbol{\theta}}|s) \propto \exp\left[-\left(\frac{(\delta\theta_p^{\hat{1}})^2}{2(\sigma_p^{\hat{1}})^2} + \frac{(\delta\theta_p^{\hat{2}})^2}{2(\sigma_p^{\hat{2}})^2}\right)\right]. \quad (4.10)$$

In these coordinates, the covariance matrix is

$$\Sigma_p^{\hat{a}\hat{b}} = \begin{bmatrix} (\sigma_p^{\hat{1}})^2 & 0 \\ 0 & (\sigma_p^{\hat{2}})^2 \end{bmatrix}. \quad (4.11)$$

Following Cutler [5], we define the error ellipse such that the probability that the source lies outside the error ellipse is e^{-1} . The semiaxes of the error ellipse are given by $\sqrt{2(\sigma_p^{\hat{1},\hat{2}})^2}$. These quantities follow from the eigenvalues of the covariance matrix (4.11); since eigenvalues are invariant under rotation, we can calculate them before performing the rotation. In terms of our original covariance matrix, the major axis $2a$ and minor axis $2b$ of the ellipse are given by

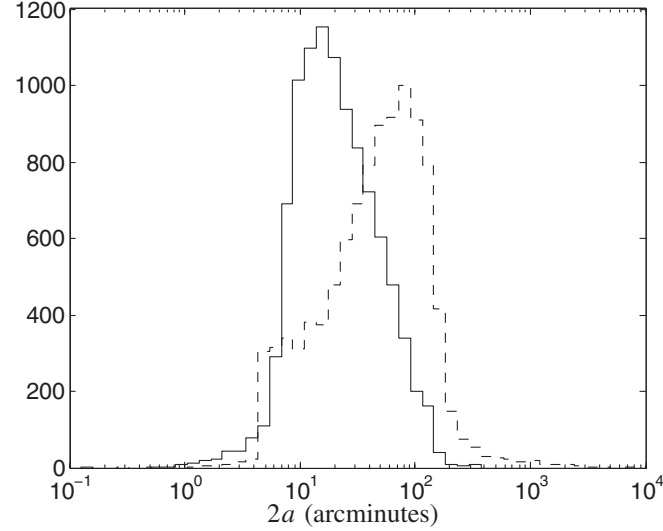


FIG. 7. Distribution of the major axis of the sky position error ellipse, $2a$, for 10^4 binaries with $m_1 = 10^6 M_\odot$ and $m_2 = 3 \times 10^5 M_\odot$ at $z = 1$. The dashed line is the precession-free calculation; the solid line includes precession. Sky position, as an extrinsic parameter, is improved somewhat indirectly by precession; therefore, the improvement is less than for the masses.

$$2 \left[\csc^2 \bar{\theta}_N \sum \bar{\mu}_N \bar{\mu}_N + \sin^2 \bar{\theta}_N \sum \bar{\phi}_N \bar{\phi}_N \right. \\ \left. \pm \sqrt{(\csc^2 \bar{\theta}_N \sum \bar{\mu}_N \bar{\mu}_N - \sin^2 \bar{\theta}_N \sum \bar{\phi}_N \bar{\phi}_N)^2 + 4(\sum \bar{\mu}_N \bar{\phi}_N)^2} \right]^{1/2}, \quad (4.12)$$

taking the plus and minus for major and minor axes, respectively. We also find the area of the error ellipse:

$$\Delta \Omega_N = \pi ab = 2\pi \sqrt{\sum \bar{\mu}_N \bar{\mu}_N \sum \bar{\phi}_N \bar{\phi}_N - (\sum \bar{\mu}_N \bar{\phi}_N)^2}. \quad (4.13)$$

Many previous analyses have reported the ellipse's area $\Delta \Omega_N$ or $\sqrt{\Delta \Omega_N}$, the side of a square of equivalent area, as the sky position error [5,7,10]. Information about the ellipse's shape, crucial input to coordinating GW observations with telescopes, is not included in such a measure. By examining both $2a$ and $2b$, this information is restored. Figure 7 shows the major axis of the error ellipse $2a$ for both the original code, with no precession, and the code including precession effects. Figure 8 shows the same for the minor axis $2b$. (Note that these figures cannot tell us which major axis is associated with which minor axis; that information is lost in the construction of the histograms.)

Compared to the code which does include precession physics, the peak of the major axis distribution is reduced by about an order of magnitude; the median of this distribution is reduced by about a factor of 2. For the minor axis, both the peak and median are reduced by about a factor of 2. The minor axis distribution also shows a long tail of very small errors. In those cases, the position would be very well constrained in one direction.

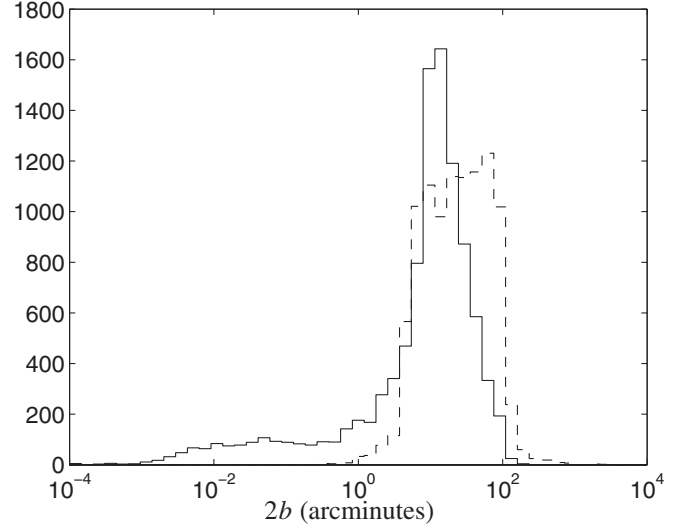


FIG. 8. Distribution of the minor axis of the sky position error ellipse, $2b$, for 10^4 binaries with $m_1 = 10^6 M_\odot$ and $m_2 = 3 \times 10^5 M_\odot$ at $z = 1$. The dashed line is the precession-free calculation; the solid line includes precession.

Finally, we examine how well distance to the binary is determined. Figure 9 compares $\Delta D_L/D_L$ both with and without precession physics taken into account. For this case, the distance error improves by a factor ~ 2 – 3 .

Table IV shows the median extrinsic errors for binaries of different mass. For comparison purposes, we include results that neglect spin precession. Binaries with the best determined parameters at this redshift have total mass $\text{several} \times 10^5 M_\odot \lesssim M_{\text{tot}} \lesssim \text{several} \times 10^6 M_\odot$ —smaller binaries are not determined quite so well due to the weakness of their signal, while larger ones are not

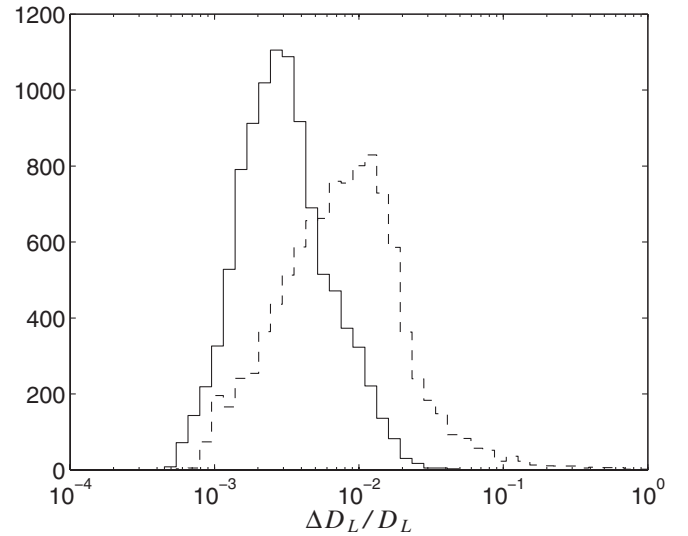


FIG. 9. Distribution of errors in the luminosity distance for 10^4 binaries with $m_1 = 10^6 M_\odot$ and $m_2 = 3 \times 10^5 M_\odot$ at $z = 1$. The dashed line is the precession-free calculation; the solid line includes precession.

TABLE IV. Median errors in extrinsic quantities for 10^4 binaries of various masses at $z = 1$, including comparisons with the “no precession” case. Note that the given major axis and minor axis are the medians for each data set and do not correspond to the same binary. However, they still represent an average sky position error ellipse in the following sense: $\sqrt{\pi ab}$, calculated using the median values of $2a$ and $2b$, differs in most cases by less than 10% from the median value of $\sqrt{\Delta\Omega_N}$ calculated from the covariance matrix and (4.13).

$m_1(M_\odot)$	$m_2(M_\odot)$	$2a$ (arcmin) (no precession)	$2a$ (arcmin) (precession)	$2b$ (arcmin) (no precession)	$2b$ (arcmin) (precession)	$\Delta D_L/D_L$ (no precession)	$\Delta D_L/D_L$ (precession)
10^5	10^5	70.9	15.5	30.9	8.30	0.0104	0.002 12
3×10^5	10^5	60.8	9.98	26.5	5.42	0.009 05	0.001 38
3×10^5	3×10^5	52.9	13.8	23.1	7.36	0.007 90	0.001 95
10^6	10^5	55.8	17.7	26.3	6.73	0.008 56	0.002 69
10^6	3×10^5	49.7	19.2	23.7	11.2	0.007 70	0.002 89
10^6	10^6	50.7	24.4	23.9	13.3	0.007 74	0.003 47
3×10^6	3×10^5	51.8	18.4	26.8	7.42	0.008 42	0.002 78
3×10^6	10^6	62.8	18.6	32.4	10.8	0.0103	0.002 81
3×10^6	3×10^6	87.8	27.4	46.7	15.4	0.0159	0.003 98
10^7	10^6	98.8	23.3	52.7	11.4	0.0177	0.003 42
10^7	3×10^6	187	27.8	88.8	15.2	0.0301	0.004 00
10^7	10^7	396	63.0	179	31.3	0.0606	0.0246

TABLE V. Median errors in extrinsic quantities for 10^4 binaries of various masses at $z = 3$.

$m_1(M_\odot)$	$m_2(M_\odot)$	$2a$ (arcmin) (no precession)	$2a$ (arcmin) (precession)	$2b$ (arcmin) (no precession)	$2b$ (arcmin) (precession)	$\Delta D_L/D_L$ (no precession)	$\Delta D_L/D_L$ (precession)
10^5	10^5	228	47.5	98.7	25.9	0.0339	0.006 60
3×10^5	10^5	205	54.1	90.9	28.0	0.0308	0.007 75
3×10^5	3×10^5	190	88.4	86.5	48.7	0.0290	0.0129
10^6	10^5	205	73.7	108	28.6	0.0337	0.0112
10^6	3×10^5	199	72.5	97.9	41.7	0.0310	0.0107
10^6	10^6	265	102	134	55.5	0.0444	0.0143
3×10^6	3×10^5	266	75.4	141	33.4	0.0442	0.0112
3×10^6	10^6	404	87.5	208	48.6	0.0714	0.0127
3×10^6	3×10^6	777	156	366	81.7	0.125	0.0267
10^7	10^6	1040	142	489	74.8	0.166	0.0229
10^7	3×10^6	2050	232	908	123	0.309	0.0854
10^7	10^7	6200	2130	2660	630	0.903	4.81

TABLE VI. Median errors in extrinsic quantities for 10^4 binaries of various masses at $z = 5$. Again, the results for the highest masses are essentially meaningless—the parameters are completely undetermined.

$m_1(M_\odot)$	$m_2(M_\odot)$	$2a$ (arcmin) (no precession)	$2a$ (arcmin) (precession)	$2b$ (arcmin) (no precession)	$2b$ (arcmin) (precession)	$\Delta D_L/D_L$ (no precession)	$\Delta D_L/D_L$ (precession)
10^5	10^5	383	100	168	53.5	0.0573	0.0142
3×10^5	10^5	359	136	167	78.0	0.0548	0.0203
3×10^5	3×10^5	343	171	170	96.1	0.0549	0.0252
10^6	10^5	372	133	192	53.9	0.0608	0.0202
10^6	3×10^5	434	133	222	76.2	0.0704	0.0198
10^6	10^6	624	199	325	112	0.113	0.0289
3×10^6	3×10^5	624	162	334	78.5	0.114	0.0237
3×10^6	10^6	1230	196	587	108	0.201	0.0282
3×10^6	3×10^6	2430	405	1100	205	0.379	0.123
10^7	10^6	4300	468	1910	262	0.653	0.159
10^7	3×10^6	9360	1690	4010	638	1.37	2.52
10^7	10^7	70 700	2.58×10^6	29 600	263 000	10.1	9010

determined so well because they radiate fewer cycles in band. We also see again that unequal mass binaries give better results than equal mass binaries due to the impact of mass ratio on precession effects. Overall, we find that the major axis of the error ellipse is on the order of 10 arcminutes for low mass and several tens of arcminutes for higher mass, while the minor axis is a factor of 2 smaller. This represents an improvement by a factor $\sim 2-6$ over the “no precession” case. The distance errors are on the order of 0.1%–0.4% for most masses, a factor of $\sim 2-7$ improvement.

Tables V and VI show the same results for higher redshift. We see the same trends as at $z = 1$, but with some degradation in numerical value. The sky position errors reach a degree or more in the major axis and several tens of arcminutes up to a degree or two in the minor axis. The distance errors are on the order of 1 to several percent for most masses. At the highest masses, we again see that these parameters are essentially undetermined and that precession makes things worse by requiring extra parameters to be fit.

V. SUMMARY AND CONCLUSIONS

The general relativistic precession of black holes in binary systems can have a strong influence on the binary’s dynamics [29,50] and thus upon the GWs that it generates. It has been known for some time that it will be necessary to take these dynamics into account in order to detect these black holes in noisy detector data [19–25]; clearly, taking these dynamics into account will be just as (if not more) important for the complementary problem of determining the parameters which characterize a detected system. Vecchio [26] first demonstrated that, by taking into account precession physics, quite a few near degeneracies among binary source parameters can be broken, making our estimates for how accurately they can be determined more optimistic. This analysis largely confirms and extends Vecchio’s pioneering work. By taking the equations of motion to higher order to include spin-spin couplings, and by surveying measurement accuracy as a function of mass ratio, we have found that the improvement noted by Vecchio holds rather broadly. The degeneracy breaking due to precession physics is a rather robust phenomenon.

Two conclusions from this work are particularly important with regard to the astrophysical reach of future LISA measurements. The first is that modeling spin-precession physics makes it possible to determine the magnitudes of the spins of the black holes which constitute the binary. If the spins are rapid, they can be measured quite accurately (as good as 0.1% accuracy for high spin, low redshift systems) due to the strong modulation imposed on the signal by their interaction. Coupled with the fact that the black hole masses can likewise be measured with good precision, this suggests that LISA will be a valuable tool for tracking the evolution of both mass and spin over cosmic

time. Such observations could provide a direct window into the growth of cosmological structures. Measuring spin may also make it possible to indirectly test the black hole area theorem [62]. The requirement that black hole area can only grow implies a consistency relation between the initial and final masses and spins. By measuring the initial masses and spins through the inspiral, and the mass and spin of the merged remnant hole through the ringdown waves [38,39], we can check this consistency relation in a manner analogous to the mass loss test proposed in [63]. We intend to investigate whether this test is feasible in future work.

Second, we confirm Vecchio’s result that precession breaks degeneracies between the angles which determine a binary’s orientation and its position on the sky, improving the accuracy with which sky position can be fixed using GWs alone. At low redshift ($z \sim 1$), we find that sources can be localized to within an ellipse whose major axis is typically ~ 10 – a few $\times 10$ arcminutes across and whose minor axis is typically a factor ~ 2 smaller. This is small enough that searching the GW pixel for an electromagnetic counterpart to the merger event should not be too arduous a task [35]. For mergers at higher redshift, the waves weaken and the source is not so well localized. The field which would need to be searched for sources at $z \sim 3-5$ is typically about a degree to a few degrees across in the long axis and tens of arcminutes to a degree or two in the short direction—a rather more difficult challenge, but not hopeless. We intend to more thoroughly investigate the nature of localization with spin precession, including how the pixel evolves with observation time up to final merger, in future work.

As mentioned in the Introduction, our analysis makes many assumptions and approximations which are likely to affect our results; a goal of future work will be to lift these approximations. One major concern is the Gaussian approximation we have taken to the likelihood function. As already discussed, this approximation is known to be good when the SNR is “large” [8,28]; however, it is not apparent what large really means, particularly given that we are fitting for 15 parameters. Lifting this simplifying approximation can be done by simply computing the likelihood function (3.9) directly and examining how well parameters are thereby determined. In the context of GW measurements, Markov Chain–Monte Carlo techniques have been investigated and found to be very useful [64–66]; the application of these techniques to LISA measurement problems is now being rather actively investigated [67–69].

Because we have used the Gaussian approximation (among other simplifications taken in this analysis), we cannot claim that this analysis gives a definitive statement about the accuracy with which LISA could measure binary black hole source parameters. However, it is certainly *indicative* of the accuracy which we expect LISA to achieve. In particular, we are confident that the trends we

have seen as parameters are varied (e.g., masses, redshift, spin magnitude) are robust. Most importantly, it is very clear that the influence of spin-induced precession upon the measured waveform allows parameters to be measured to greater accuracy than before.

ACKNOWLEDGMENTS

This work benefited greatly from discussions with and feedback from members of the LISA International Science Team, especially Neil Cornish, E. Sterl Phinney, and Thomas Prince. We also thank Bence Kocsis for very useful discussions about parametrizing the sky position

error ellipse, Shane Larson for providing code to process his noise files, and Jeremy Schnittman for helpful comments about the precession equations. We are especially grateful to Emanuele Berti for discussions regarding integrators, which led to a drastic improvement in the ability of our code to perform large Monte Carlo surveys, as well as many insightful comments about this manuscript. This work was supported by NASA Grant No. NAGW-12906 and NSF Grant No. PHY-0449884. S. A. H. gratefully acknowledges the support of the MIT Class of 1956 Career Development fund.

-
- [1] L. Ferrarese and D. Merritt, *Astrophys. J. Lett.* **539**, L9 (2000).
 - [2] K. Gebhardt *et al.*, *Astrophys. J. Lett.* **539**, L13 (2000).
 - [3] See for example P.F. Hopkins, L. Hernquist, T.J. Cox, T. Di Matteo, B. Robertson, and V. Springel, *Astrophys. J. Suppl. Ser.* **163**, 1 (2006).
 - [4] M. Volonteri, P. Madau, and F. Haardt, *Astrophys. J.* **593**, 661 (2003).
 - [5] C. Cutler, *Phys. Rev. D* **57**, 7089 (1998).
 - [6] S. A. Hughes, *Mon. Not. R. Astron. Soc.* **331**, 805 (2002).
 - [7] E. Berti, A. Buonanno, and C. M. Will, *Phys. Rev. D* **71**, 084025 (2005).
 - [8] C. Cutler and É.É. Flanagan, *Phys. Rev. D* **49**, 2658 (1994).
 - [9] E. Poisson and C. M. Will, *Phys. Rev. D* **52**, 848 (1995).
 - [10] D. E. Holz and S. A. Hughes, *Astrophys. J.* **629**, 15 (2005).
 - [11] K. S. Thorne, R. H. Price, and D. A. MacDonald, *Black Holes: The Membrane Paradigm* (Yale University Press, New Haven, CT, 1986).
 - [12] K. S. Thorne and J. B. Hartle, *Phys. Rev. D* **31**, 1815 (1985).
 - [13] Discussion and references can be found at the Gravity Probe B website, <http://einstein.stanford.edu>.
 - [14] R. D. Blandford and R. L. Znajek, *Mon. Not. R. Astron. Soc.* **179**, 433 (1977).
 - [15] D. L. Meier, *New Astron. Rev.* **47**, 667 (2003).
 - [16] C. S. Reynolds and M. A. Nowak, *Phys. Rep.* **377**, 389 (2003).
 - [17] S. A. Hughes and R. D. Blandford, *Astrophys. J. Lett.* **585**, L101 (2003).
 - [18] H. R. Schmitt, J. E. Pringle, C. J. Clarke, and A. L. Kinney, *Astrophys. J.* **575**, 150 (2002).
 - [19] A. Buonanno, Y. Chen, and M. Vallisneri, *Phys. Rev. D* **67**, 104025 (2003).
 - [20] Y. Pan, A. Buonanno, Y. Chen, and M. Vallisneri, *Phys. Rev. D* **69**, 104017 (2004).
 - [21] A. Buonanno, Y. Chen, Y. Pan, and M. Vallisneri, *Phys. Rev. D* **70**, 104003 (2004).
 - [22] A. Buonanno, Y. Chen, Y. Pan, H. Tagoshi, and M. Vallisneri, *Phys. Rev. D* **72**, 084027 (2005).
 - [23] P. Grandclément, V. Kalogera, and A. Vecchio, *Phys. Rev. D* **67**, 042003 (2003).
 - [24] P. Grandclément and V. Kalogera, *Phys. Rev. D* **67**, 082002 (2003).
 - [25] P. Grandclément, M. Ihm, V. Kalogera, and K. Belczynski, *Phys. Rev. D* **69**, 102002 (2004).
 - [26] A. Vecchio, *Phys. Rev. D* **70**, 042001 (2004).
 - [27] L. Barack and C. Cutler, *Phys. Rev. D* **69**, 082005 (2004).
 - [28] L. S. Finn, *Phys. Rev. D* **46**, 5236 (1992).
 - [29] T. A. Apostolatos, C. Cutler, G. J. Sussman, and K. S. Thorne, *Phys. Rev. D* **49**, 6274 (1994).
 - [30] G. Faye, L. Blanchet, and A. Buonanno, gr-qc/0605139 [*Phys. Rev. D* (to be published)].
 - [31] L. Blanchet, A. Buonanno, and G. Faye, gr-qc/0605140 [*Phys. Rev. D* (to be published)].
 - [32] R. Porto and I. Z. Rothstein, gr-qc/0604099.
 - [33] P. J. Armitage and P. Natarajan, *Astrophys. J. Lett.* **567**, L9 (2002).
 - [34] M. Milosavljević and E. S. Phinney, *Astrophys. J. Lett.* **622**, L93 (2005).
 - [35] B. Kocsis, Z. Frei, Z. Haiman, and K. Menou, *Astrophys. J.* **637**, 27 (2006).
 - [36] D. N. Spergel *et al.*, astro-ph/0603449.
 - [37] F. Echevarria, *Phys. Rev. D* **40**, 3194 (1989).
 - [38] O. Dreyer, B. Kelly, B. Krishnan, L. S. Finn, D. Garrison, and R. Lopez-Aleman, *Classical Quantum Gravity* **21**, 787 (2004).
 - [39] E. Berti, V. Cardoso, and C. M. Will, *Phys. Rev. D*, **73**, 064030 (2006).
 - [40] F. Pretorius, *Phys. Rev. Lett.* **95**, 121101 (2005).
 - [41] M. Campanelli, C. O. Lousto, P. Marronetti, and Y. Zlochower, *Phys. Rev. Lett.* **96**, 111101 (2006).
 - [42] J. G. Baker, J. Centrella, D. Choi, M. Koppitz, and J. van Meter, *Phys. Rev. Lett.* **96**, 111102 (2006).
 - [43] P. C. Peters, *Phys. Rev.* **136**, B1224 (1964).
 - [44] L. Blanchet, *Living Rev. Relativity* **9**, 4 (2006).
 - [45] L. E. Kidder, C. M. Will, and A. G. Wiseman, *Phys. Rev. D* **47**, R4183 (1993).
 - [46] L. Blanchet, T. Damour, B. R. Iyer, C. M. Will, and A. G. Wiseman, *Phys. Rev. Lett.* **74**, 3515 (1995).

- [47] L. E. Kidder, Phys. Rev. D **52**, 821 (1995).
- [48] C. M. Will and A. G. Wiseman, Phys. Rev. D **54**, 4813 (1996).
- [49] R. W. Hellings and T. A. Moore, Classical Quantum Gravity **20**, S181 (2003).
- [50] J. D. Schnittman, Phys. Rev. D **70**, 124020 (2004).
- [51] A. Sesana, F. Haardt, P. Madau, and M. Volonteri, Astrophys. J. **623**, 23 (2005).
- [52] N. J. Cornish and L. J. Rubbo, Phys. Rev. D **67**, 022001 (2003).
- [53] L. J. Rubbo, Ph.D. thesis, Montana State University, 2004.
- [54] É. É. Flanagan and S. A. Hughes, New J. Phys. **7**, 204 (2005).
- [55] S. L. Larson, W. A. Hiscock, and R. W. Hellings, Phys. Rev. D **62**, 062001 (2000).
- [56] The sensitivity curve generator can be found online at <http://www.srl.caltech.edu/~shane/sensitivity/>.
- [57] A. J. Farmer and E. S. Phinney, Mon. Not. R. Astron. Soc. **346**, 1197 (2003).
- [58] G. Nelemans, L. R. Yungelson, and S. F. Portegies Zwart, Astron. Astrophys. **375**, 890 (2001).
- [59] N. J. Cornish, gr-qc/0304020.
- [60] W. H. Press, S. A. Teukolsky, W. T. Vetterling, and B. P. Flannery, *Numerical Recipes in C* (Cambridge University Press, Cambridge, 1992).
- [61] D. W. Hogg, astro-ph/9905116.
- [62] S. W. Hawking, Phys. Rev. Lett. **26**, 1344 (1971).
- [63] S. A. Hughes and K. Menou, Astrophys. J. **623**, 689 (2005).
- [64] N. Christensen and R. Meyer, Phys. Rev. D **64**, 022001 (2001).
- [65] N. Christensen, R. J. Dupuis, G. Woan, and R. Meyer, Phys. Rev. D **70**, 022001 (2004).
- [66] R. Umstätter, R. Meyer, R. J. Dupuis, J. Veitch, G. Woan, and N. Christensen, Classical Quantum Gravity **21**, S1655 (2004).
- [67] N. J. Cornish and J. Crowder, Phys. Rev. D **72**, 043005 (2005).
- [68] N. J. Cornish and E. K. Porter, Classical Quantum Gravity **23**, S761 (2006).
- [69] N. J. Cornish and E. K. Porter, gr-qc/0605135.